1-1-2013

Effect of Nanoparticle Size, Support, and Potassium Dopant on Ruthenium Activity for Levulinic Acid (LA) Hydrogenation to γ-Valerolactone (GVL)

Shuo Cao
University of South Carolina

Effect of Nanoparticle Size, Support, and Potassium Dopant on Ruthenium Activity for Levulinic Acid (LA) Hydrogenation to γ-Valerolactone (GVL)

by

Shuo Cao

Bachelor of Science
Wuhan Institute of Technology, Wuhan, China, 2006

Submitted in Partial Fulfillment of the Requirement

For the Degree of Master of Science in

Chemical Engineering

College of Engineering and Computing

University of South Carolina

2013

Accepted by:

John R. Regalbuto, Major Professor

John R. Monnier, Committee Member

Jason, Hattrick-Simpers Committee Member

John Weidner, Committee Member

Lacy Ford, Vice Provost and Dean of Graduate Studies

ACKNOWLEDGEMENT

It is a pleasure to take this opportunity to thank the many wonderful people who made it possible for me to complete my Masters program. First and foremost, I would like to express my deep and sincere gratitude to my advisor, Professor. John R. Regalbuto. At the low point of my life, he offered the opportunity to perform and improve myself. He is my hero and always provides valuable instruction, guidance and encouragement to help me overcome all the difficulties I faced in my research and course study. He is my life-model and his behavior teaches me how to deal with many different kinds of affairs. His patience and trust makes me confident. I am truly lucky and honored to know and work with him.

I am particularly to thank my wife, Yinhao, for standing by me and encouraging me all the time and accompanying me for the late work and weekends through the past two years in school. Thanks to her for bringing our son, Washington, to me last summer. My largest motivation to pursue my academic goal comes from them. I would also like to thank to my parents and parents-in-law. Their unconditional love and limitless capacity always cheer me up and give me a future to look forward to.

I must acknowledge my colleagues, with whom I had the pleasure to interact and collaborate. I appreciated the help, teaching, effort, enthusiasm and friendship of our group members, Hye-ran Cho, John Tengco, Jadid Samad, Kerry O'Connell, Qiuli Liu and Ritu Banerjee, as well as other group members, Abraham A Rodriguez, Weijian Diao, Yuliana Lugo Jose, YunYa Zhang, Shuai Tan and Xiaojing Sun.

I am also very grateful to Dr. John Monnier for always pushing me to think about problems deeply and become a better Chemical Engineer. His invaluable experiences and practical knowledge about science and life has helped me a lot in my research and life. I am very fortunate to have him teaching me the details of our experimental setup.

ABSTRACT

The purpose of this thesis is to study the effect of nanoparticle size, support and potassium dopant on ruthenium activity on the levulinic acid (LA) hydrogenation to γ-valeroactone (GVL). In hydrogenation, H_2 from the gas phase reactant reacts with metal atoms at the surface of particles, thus a high level of metal dispersion is critical to maximize the amount of atoms on the surface. This reaction has been widely investigated by varied metal supported catalysts and proved that Ru is the most active metal for it. However, most researchers only focused on the process, rather than the Ru particle size. Furthermore, Ru nanoparticle synthesis by various methods for other types of reactions also have been reported, yet in studies where the same method, metal precursor and metal weight loading were employed, inconsistent Ru particle sizes were obtained. Due to the important role of the metal particle size, it needs to be systematically examined and syntheses must be reproducible.

Chapter 1 provides a brief introduction to explain the purposes and importance of this research. Important theoretical concepts and descriptions are given about the reaction pathway, the preparation method of catalyst and the characterization techniques (ICP, TPR, XPS, XRD, STEM and Chemisorption) employed. A literature review is also presented.

The experimental operation is described in Chapter 2. Catalysts prepared by strong electrostatic adsorption and dry impregnation as well as commercial catalysts were used for kinetic evaluation. Ru metal precursors were deposited on low PZC support,

oxidized carbon, and high PZC support, γ-Al_2O_3. TPR is used to determine the proper reduction temperature. After H_2 reduction pretreatment, Ru particle size was characterized by XRD, STEM and chemisorption.

The results and discussion are presented in Chapter 3. In general, carbon as a support imparted higher catalytic activity than alumin. A pronounced enhancement of activity by potassium promotion was discovered. Alumina supported catalysts did not appear to exhibit a particle size effect, as the turnover frequencies calculated on the basis of chemisorption were similar to those estimated from STEM particle size; both sets of numbers did not vary significantly with particle size. On the other hand, a significant discrepancy of particle size estimates via STEM and chemisorption was discovered for the carbon supported catalysts. The unexpectedly low chemisorption uptake is postulated to arise from a decorating layer of carbon in the Ru nanoparticle surfaces. As such, nothing could be concluded about the effect of particle size on TOF for the carbon supported catalysts.

The general conclusions for these results are presented in Chapter 4 together with recommendation for future work, which will explore the optimization of amount and type (Na^+, K^+, Cs^+) of alkali promotion. In addition, bimetallic RuRe prepared by Co-SEA and Co-DI will be evaluated and compared with monometallic catalysts.

TABLE OF CONTENTS

LIST OF TABLES

LIST OF FIGURES

LIST OF ABBREVIATION

CPA	Chloroplatinic Acid
Cox	Oxidized Carbon
DI	Dry Impregnation
Γ	Adsorption Density or Surface Coverage [μmol/m^2]
GC	Gas Chromatography
GVL	γ- Valerolactone
ICP-AES	Inductively Coupled Plasma-Atomic Emission Spectrometry
IW	Incipient Wetness
LA	Levulinic Acid
PTA	Platinum Tetraammine
PZC	Point of Zero Charge
SEA	Strong Electrostatic Adsorption
SL	Surface Loading [m^2/L]
STEM	Scanning Transmission Electron Microscopy
T	Temperature [℃]
TPR	Temperature Programmed Reduction
WI	Wet Impregnation
XPS	X-Ray Photoelectron Spectroscopy
XRD	X-Ray Diffraction

Chapter 1. Introduction

With the worldwide petroleum resources dwindling, it is urgent to find renewable replacements for petroleum-derived products to accelerate the transition to renewable fuels to adapt to the increasing demand of our society. Several recent reports have underscored that biomass feedstocks are heavily used for the green catalytic conversion to renewable fuels and chemicals.[1, 2]

In light of a report submitted to the US government in 2002 "The Roadmap for Biomass Technologies", it has been predicted that by 2030, 20% of transportation fuel and 25% of value added chemicals will be produced from lignocellulosic biomass which is the only carbon source capable of supplanting fossil fuels.[3] As an alternative carbon source, lignocellulosic biomass has several advantages over petroleum. First of all, lignocellulosic biomass is invaluable and has widespread worldwide availability. It is reported that 1.3 billion tons of dry biomass can be produced per year in United States alone. Furthermore, the carbon source in lignocellulosic biomass is renewable and is converted into many valued added chemicals and fuels, such as reducing sugars, furfural, various carboxylic acids including levulinic acid (LA), lactic acids, etc. There are three main components of lignocellulosic biomass: cellulose, hemicelluloses and lignin. The main challenge is the conversion of biomass feedstocks into renewable fuels.[4] For this reason, catalytic conversion of biomass has received increased attention in recent

years.[1, 5-9] Consequently, catalysts play a significant role in improving reaction rates and selectivity to the desired products.

Levulinic acid (LA) is inexpensive and can be obtained though the decomposition of cellulose feedstock: glucose. It is a well-known product of hexose acid hydrolysis and its chemical properties were reported in the literature. In addition, it is a low molecular weight carboxylic acid with a ketonic carbonyl group. Therefore, it is used as the starting material for the production of many useful C_5 based compounds such as GVL, 2-methyltetrahydrofuran (MTHF) and other derivatives.[4]

As the one of major products of plant biomass, γ-valerolactone (GVL) has attracted considerable attention because it is renewable, safe to store, and could be used as (1) precursor of gasoline and diesel fuels, such as C_8-C_{16} alkenes, C_9-C_{18} alkanes, C_9 alkanes, valeric esters, or butane isomers, (2) food additives, green solvents, mixed with conventional gasoline in a capacity similar to ethanol and (3) as an intermediate in the synthesis of many value added chemicals, such as, 1,4 pentanediol, α-methylene γ-valerolactone and pentenoate esters.[10-12] The synthesis of γ-valerolactone (GVL) commonly consists of the hydrogenation of levulinic acid (LA) using either using homogeneous or heterogeneous catalysis.[13] However, since the boiling point of GVL is about 207 ℃, which will increase the difficulty in product/catalyst separation, catalysts recovery, and recycling; thus it is not used for commercial production.[4] For this reason, homogeneous Ru catalysts have been confined in an aqueous phase in order to recycle the caatalyst effectively However, only one catalyst recycle cycle was used, which leads to a remarkable decrease in the conversion of LA. Recently, the manufacturing of GVL has mainly relied on the use heterogeneous catalysts.[11, 14] Now, the question has moved to

the pursuit of the best metal support catalyst in order to improve the conversion and selectivity.

Ru has been proven to be the most active metal for hydrogenation of aliphatic carbonyl compounds.[13, 15] Consequently, the production of GVL relies on the use Ru based heterogeneous catalysts. The large metal weight loading required for commercial production is cost prohibitive as Ru is quite expensive, increased weight loadings lead to higher capital costs. It is then imperative to reduce the Ru weight loading and improve the catalyst activity and efficiency, either by optimizing the metal dispersion or introducing a second metal to make bimetallic particles that can lead to a bimetallic effect that can increase selectivity and activity.

1.1 Catalyst Preparation Methods

A wide variety of catalyst preparation methods has been developed for satisfying the increased demand of industry as the use of catalyst in chemical processes increases. The three most common and important methods of catalyst synthesis employed for industrial production are impregnation, adsorption, and precipitation.[16] Among all preparation methods of metal supported catalyst, impregnation is the simplest, least expensive, and most prevalent. The most common types of impregnation can be classified as wet or dry. This depends on the volume of impregnating solution and the pore volume of support. If the volume of metallic precursor solution is equal to the pore volume of support, it is termed dry impregnation (DI). If the volume of impregnation solution is considerably larger, it is termed as wetness impregnation (WI). Either DI or WI is a simple method since the PH of the solution does need to be adjusted. In addition, little to no precursor will be wasted during the impregnation process and precise metal weight

loadings can be achieved. Since the PH of impregnation solution is not controlled, the PH of the metal precursor solution can change dramatically and often adjusts to the point zero charge (PZC) of the support, where no interaction occurs between metal and support sites. For this reason, it is difficult to obtain a uniform metal distribution throughout the whole support. After impregnation, drying and pretreatment steps are used to remove the ligands from the metal precursor and reduce the metal to metallic state. During this pretreatment process if no metal –support interaction occurs the metal complex will be very mobile and tend to sinter, which will result in the increase of metal particle size.[17]

Adsorption has recently been used for heterogeneous catalyst impregnation. A land mark work reported by Brunelle was demonstrated that the adsorption of noble metal complexes onto common oxides supports was essentially columbic in nature.[18] In principle, adsorption is an impregnation method that creates a strong electrostatic interaction between the ionic metal precursor and hydroxyl groups on the surface of support. This strong interaction can ensure the metal precursor strongly adsorbs on the surface of support leading to increased metal particle dispersion.[19]

The mechanism of Strong Electrostatic Adsorption (SEA) is illustrated in Figure 1.1.[20] An oxide surface contains the hydroxyl groups that can be protonated or deprotonated, depending on the pH of metal precursor solution. In order to understand this process the point zero charge (PZC) will be introduced, where the pH of the surface hydroxyl groups are neutral. At pH values below the PZC, the surface hydroxyl groups protonate and become positively charged. The surface can absorb anionic metal precursors and in the opposite way at pH values above the PZC, the surface hydroxyl groups become deprotonated and become negatively charged, the surface can adsorb

cationic metal precursors.[21-23] The PZC of the support can be acidic or basic. For instance, the PZC of SiO_2 is about 4,[24] Al_2O_3 is about 8.[21] Carbon is a special case; the PZC can be changed by the increasing or decreasing the amount of oxygen functional groups on the surface at mild or rigorous oxidation conditions. The PZC measurement of different carbons is presented in Fig.1.2.The PZC of Norit SX-ULTRA is around 8.1. However, the PZCs of Darco KB-B and Norit CA-1 are 5.0 and 2.5, respectively.[25-28] A low PZC support has a negatively charged surface, which can absorb cationic metal precursors, such as platinum tetraammine (PTA) $[Pt(NH_3)_4]^{2+}$. High PZC supports have positively charged surface, which can absorb anionic metal precursors, such as chloroplatinic acid (CPA) $[PtCl_6]^{2-}$. The greatest benefit of SEA is that a monolayer of adsorbed metal complexes on the surface can be reduced to form metal particles at very high dispersion.[29]

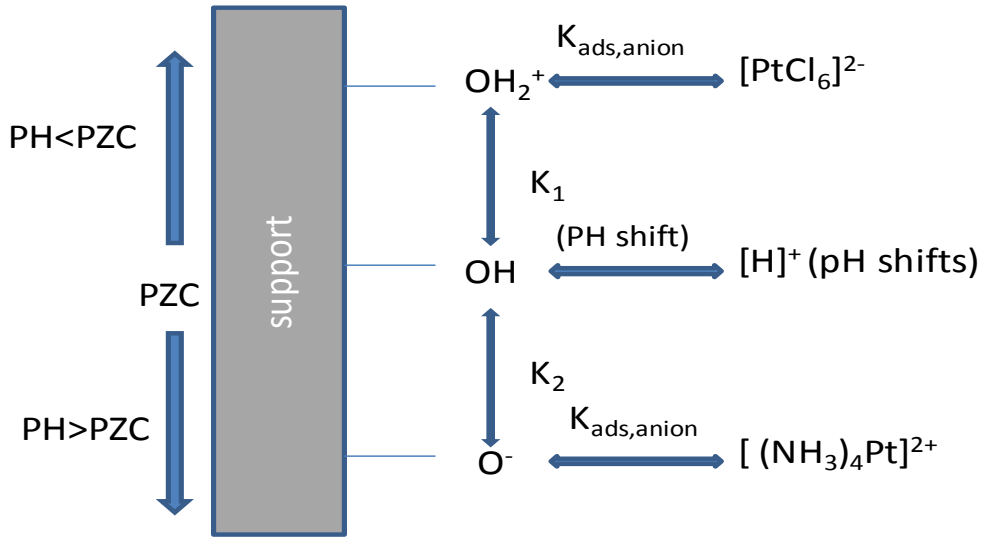

Figure 1.1 Mechanism of Strong Electrostatic Adsorption (SEA) for CPA and PTA system.[20]

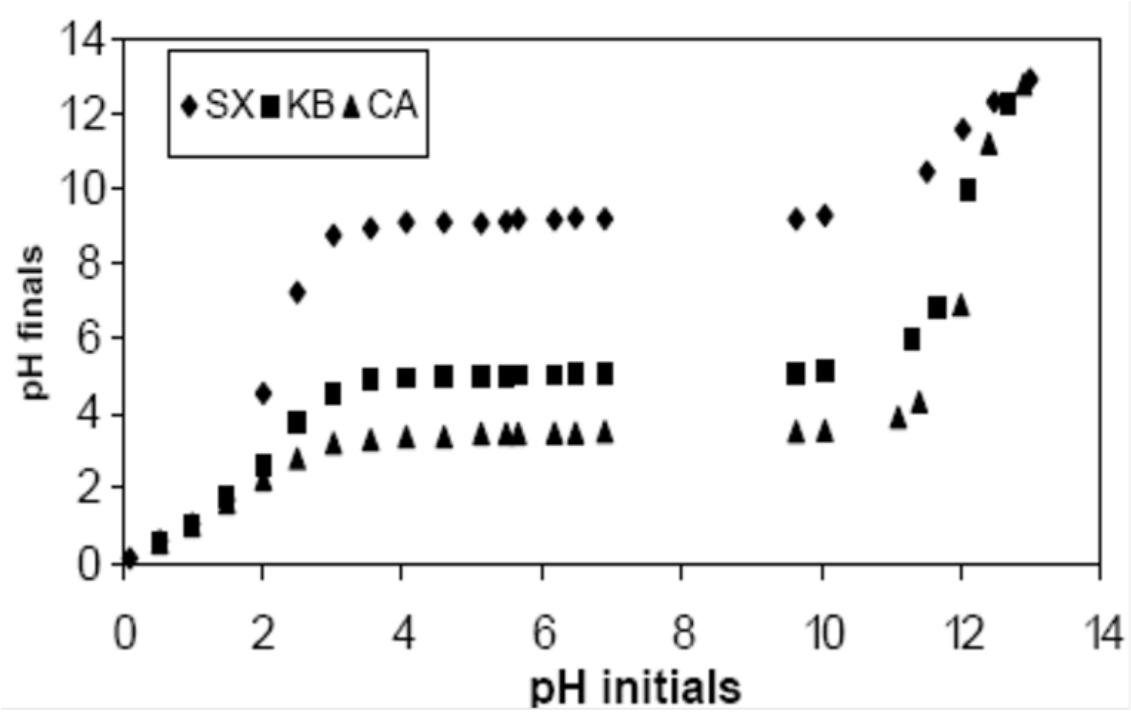

Figure 1.2 PZC measurements of activated carbons at SL=60000m^2/L.[28]

As the discussion above, the PZC measurement of the support is the first step to perform the method of SEA. To determine the PZC of a support, we can plot the PH shifts of the solution before and after contact with the support at high surface loading (SL),[30] This is the surface area of the support per volume of solution,

$$Surface\ loading\ \left(\frac{m2}{L}\right) = \frac{\left[Mass\ of\ Support(g) * Surface\ area\ of\ support\left(\frac{m2}{g}\right)\right]}{volume\ of\ solution\ (L)} \quad (1\text{-}1)$$

In the plot shown in Fig 1.3, a plateau is observed and corresponds to the PZC value of the support. Based on the PZC information of support, proper precursor can be selected for SEA method.

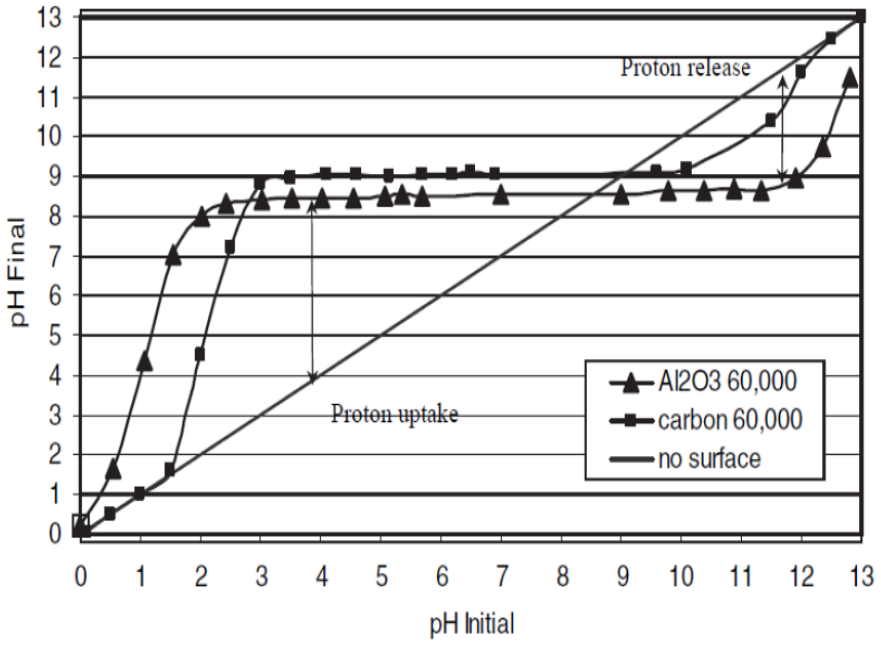

Figure 1.3 PZC measurement for a carbon and an alumina supports.[31]

To find the optimal pH to obtain the maximum metal adsorbed on the support, a metal uptake survey should be performed. The varied concentration of metal precursor adsorbed onto the support at a desired surface loading though various pH values is exemplified in Fig.1.4 a and b.[28] A sharp volcano peak is observed. Fig.1.4 a shows CPA uptake over high PZC carbon (PZC=9.1), where the metal surface density is very low at pH=9.1. Fig.1.4 b shows PTA uptake over low PZC carbon (PZC=4), when pH=4, the metal surface hydroxyl density is zero. According to the mechanism of SEA no metal adsorption occurred when the pH of the metal precursor solution is equal to the PZC of the support for both cases. In addition, the maximum uptake appears at the range from 11 to 13 for PTA, 2 to 3 for CPA. The Revised Physical Adsorption (RPA) model has been developed to explain the principle of the adsorption.[32, 33]

Due to the strong interaction between the metal precursor and the support highly dispersed metal particles can form after H_2 reduction. Strong electrostatic adsorption has its limitations, that is, the electrostatic attraction only allows one monolayer of metal precursor to be deposited onto the surface of the support due to the presence of a hydration sheath around the metal complex. Fig 1.5 [31] shows how the hydration sheath impacts the maximum of metal loading on the support. The hydration sheaths around the metal set a boundary to the amount of molecules that can be positioned next to each other in a closed packed fashion.

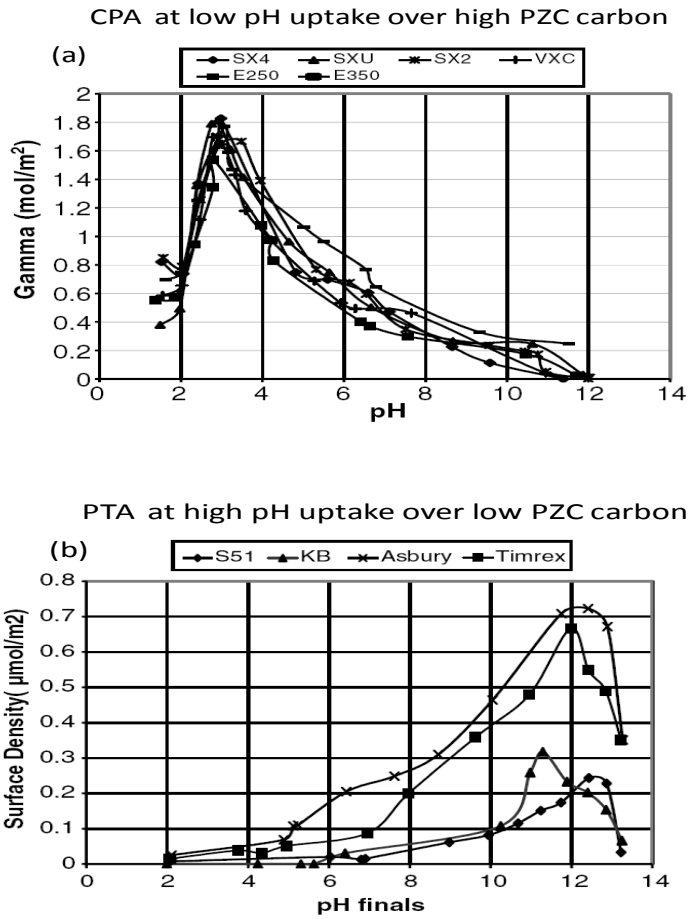

Figure 1.4 (a) Final pH vs. uptake (Γ) plot for CPA on high PZC carbon (PZC=9.1) (b) Final pH vs. uptake (Γ) plot for PTA on low PZC carbon (PZC=4).[28]

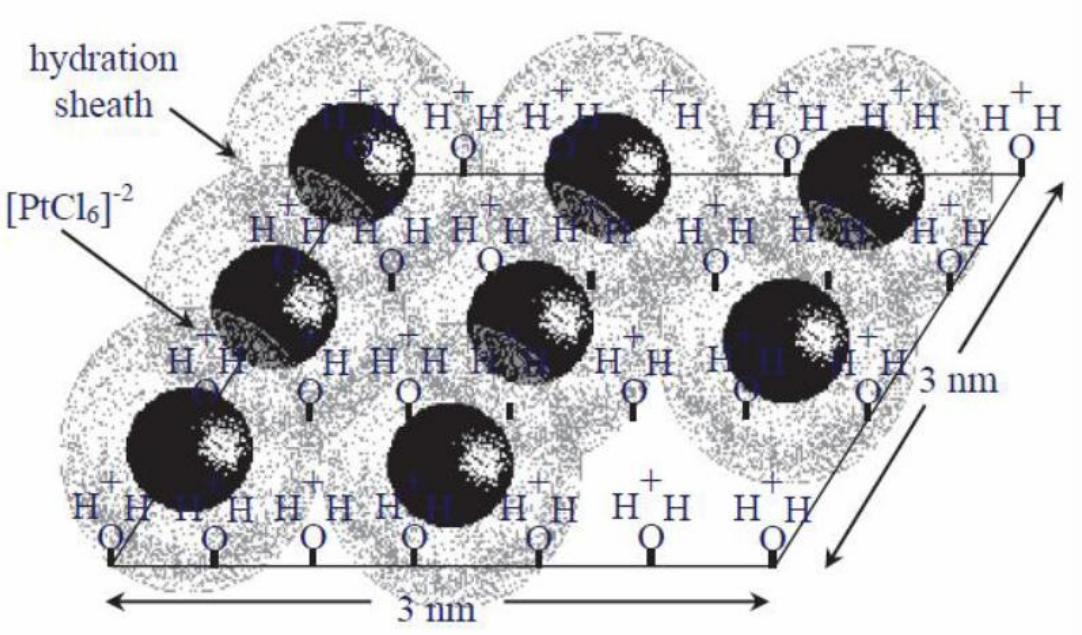

Figure.1.5 Monolayer coverage of CPA.[31]

1.2 The reaction pathway of LA hydrogenation to GVL

The reaction pathway for the hydrogenation of LA into GVL was reported by Liu and presented in Fig.1.6.[34] There are three possible pathways for this reaction, the first possible pathway was chemisorption of hydrogen and LA. Hydrogen following the division of the H diatom, which are transferred separately, were adsorbed on the surface of Ru to form the bond between Ru and hydrogen, the two atoms and then LA was adsorbed on the surface of Ru by the combination of Ru with carbonylic C and O atoms. The first hydrogen atom was added to the LA to generate an intermediate to link to the surface of Ru by a σ-bond formed between carbon and Ru followed by adding another H atom to give rise to the formation of γ-hydroxyvaleric acid. Finally, γ-hydroxyvaleric acid forms GVL by dehydrogenation. The second possible pathway was to form GVL's reciprocal transformation, pseudo-LA. The last possible pathway was that the LA reacted

with methanol to generate methyl levulinate and counter–reaction of the esterification reaction also takes place with the release of LA. However, 1,4 dixoane was used as the solvent in our system. Therefore, only the two former pathways are considered for our case.

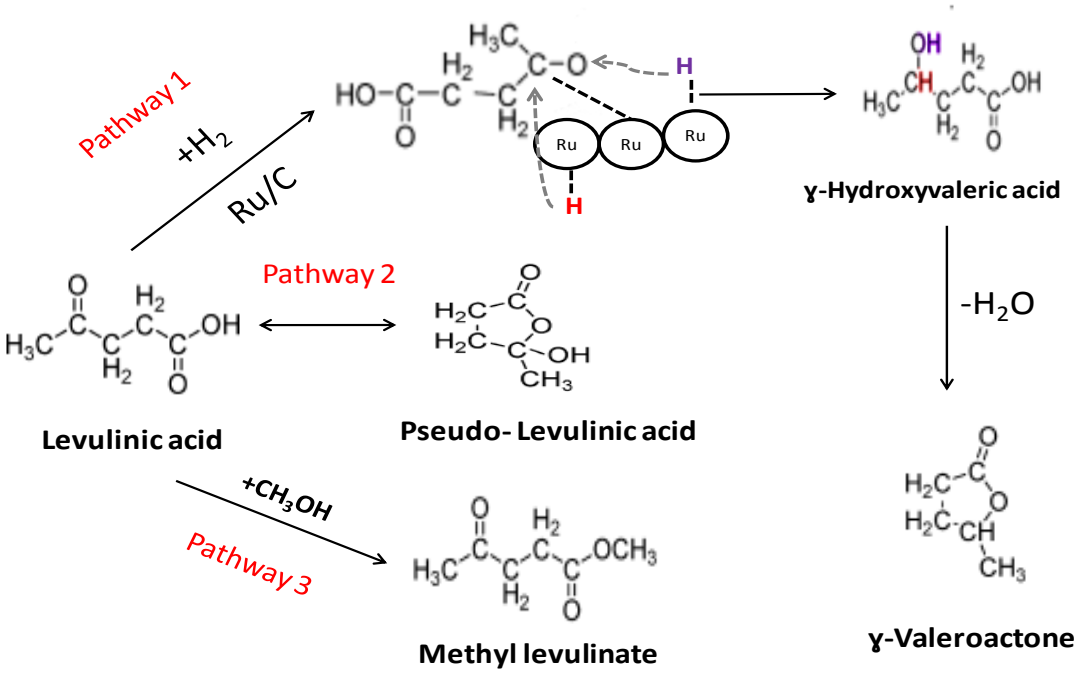

Figure. 1.6 Schematic diagram of LA hydrogenation to GVL reaction pathway.[34]

1.3 Literature Review

The hydrogenation of LA into GVL with Ru supported on either carbon or Al_2O_3 catalysts has been reported by several groups [10, 15, 35, 36] and carbon shows higher activity than Al_2O_3.[37, 38] Unfortunately, to our knowledge, the mechanism is not clear. In general, the smaller metal particle size leads to higher metal utilization during the reaction. Therefore, metal particle size plays an important role in the reaction. Ru particle

sizes used for LA hydrogenation into GVL as well as Ru nanoparticle preparation was summarized in Table 1.1 and in Table 1.2, respectively.

Supported metal catalyst has been widely studied for the LA hydrogenation to GVL. Various metals supported on carbon were screened to find the most active metal for GVL synthesis by Manzer.[15] All catalysts were prepared by dry impregnation and the reaction is performed in 1.4 dioxane solvent at 150℃, with 800 psi H_2 pressure. Among the catalysts screened, Ru/C shows the highest activity yielding the highest conversion (80%). Ir, Rh, and Pd give the moderate activity (～35%). However, low LA conversions were obtained by Pt, Re and Ni system (less than 15%). Further studies on the effect of metal and support are performed at milder condition by Hengne, all catalysts were also prepared by dry impregnation. Ru/C again gave the highest GVL conversion and carbon gives higher activity than Al_2O_3. Based on the reported finding, Ru/C is very active for GVL synthesis. Ru/C commercial catalysts were extensively utilized to study the reaction process at different conditions by many researchers. However, Ru particle size was reported by few groups (～4nm), but not in the majority of the LA hydrogenation references.

Due to the important role of metal particle size in the reaction, Ru nanoparticle supported on carbon and Al_2O_3 preparation methods are summarized in Table 1.2, where wet impregnation is employed as the most common method to prepare Ru nanoparticle. Ru loading (1%, 2%, 5%) and the influence on the particle size was studied by Gavlvagno,[43] who reported that particle size increases as the Ru loading increases. However, it is inconsistent with the claim made by Zheng,[45] who prepared the same catalysts series as Gavlvagno did and observed the reverse phenomena. The same trend is

also observed for Al_2O_3 support, even though the same precursor and methods were used for the preparation, very different particle size was obtained. Therefore, wetness impregnation is not reproducible and not necessarily the optimal method to prepare Ru nanoparticles.

The purpose of this thesis is to use strong electrostatic adsorption to synthesize reproducible and optimal Ru particle size as well as study effect of particle size, support and potassium dopant on ruthenium activity for LA hydrogenation of GVL.

Table. 1.1 Summary of Ru particle size obtained by varied types of catalyst preparation methods for LA hydrogenation to GVL.

Support	Metal	Metal wt%	Method	PZ (nm)	Precursor	Condition	LA Conv./ GVL sel./GVL yield	Rates (mol GVL/g metal/h)	Ref.
Carbon	Ru	5	DI	n.r.	n.r.	150℃, 800psi H_2,2h 1,4-Dixoane	80%/90%/--	n.r.	[15]
Carbon	Pt	5	DI	n.r.	n.r.		12%/80%/--	n.r.	
Carbon	Pd	5	DI	n.r.	n.r.		30%/90%/--	n.r.	
Carbon	Ir	5	DI	n.r.	n.r.		39%/95%/--	n.r.	
Carbon	Re	5	DI	n.r.	n.r.		8%/80%/--	n.r.	
Carbon	Rh	5	DI	n.r.	n.r.		29%/94%/--	n.r.	
Carbon	Ni	5	DI	n.r.	n.r.		1%/10%/--	n.r.	
Carbon	Ru	5	DI	n.r.	$RuCl_3$	130 ℃,500psi H_2 2h, MeOH	95%/91%/--	n.r.	[36]
Carbon	Pt	5	DI	n.r.	$RuCl_3$		18%/47%/--	n.r.	
Carbon	Pd	5	DI	n.r.	$RuCl_3$		14%/65%/--	n.r.	
SiO_2	Ru	5	DI	n.r.	$RuCl_3$		15%/89%/--	n.r.	
Al_2O_3	Ru	5	DI	n.r.	$RuCl_3$		7%/47%/--		
Carbon	Ru	5	n.r.	n.r.	n.r.	130 ℃,172psi H_2 2.7h,MeOH	92%/99%/--	2.92	[34a]
Carbon	Pd	5	n.r.	n.r.	n.r.		18%/39%/--	n.r.	
Carbon	Ru	5	Com.	n.r.	n.r.	130 ℃,172psi H_2 2.7h, 1,4 Dioxane	4.3%/0%/--	n.r.	[34b]
Carbon	Ru	n.r.	Immo.	n.r.	$RuCl_3$	150 ℃,580psi H_2 1h,formic acid	--/--/67%	n.r.	[11]
TiO_2	Ru	n.r.	Immo.	n.r.	$RuCl_3$		--/--/63%	n.r.	
Carbon	Ru	5	Com.	n.r.	n.r.	70 ℃,435psi	100%/99.9%/--	n.r.	[38]

Al_2O_3	Ru	5	Com.	n.r.	n.r.	H_2,3h, water with acid co-catalyst	57%/96.7%/--	n.r.	
Carbon	Ru	5	Com.	n.r.	n.r.	130 ℃,174psi H_2 2.7h,MeOH	99%/85.3%/84.4%	1.08	
Carbon	Ru	5	Com.	n.r.	n.r.	130 ℃,174psi H_2 2.7h,Ethanol	75.5%/81.5%/61.1%	0.79	
Carbon	Ru	5	Com.	n.r.	n.r.	130 ℃,174psi H_2 2.7h,Butanol	48.6%/81.7%/39.7%	0.49	
Carbon	Ru	5	Com.	n.r.	n.r.	130 ℃,174psi H_2 2.7h,1,4 Dioxane	98.8%/97.7/95.9%	1.24	[37]
Carbon	Ru	5	Com.	n.r.	n.r.	130 ℃,290psi H_2 2.7h,Butanol	100%98.3%/98.3%	1.24	
Carbon	Ru	5	Com.	n.r.	n.r.	130 ℃,174psi H_2 2.7h,water	99.5%/ 86.6%/86.2%	1.08	
Al_2O_3	Ru	5	Com.	n.r.	n.r.	130 ℃,174psi H_2 2.7h,Ethanol	37.7%/85.8%/32.3%	0.98	
SiO_2	Ru	5	Com.	n.r.	n.r.	130 ℃,174psi H_2 2.7h,Ethanol	82.9%/92.8%/77%	0.98	
Carbon	Ru	5	Com.	n.r.	n.r.	150 ℃,508psi H_2 --solvent free	---/---/---	0.0034	[39]
Carbon	Ru	5	Com.	<4.0	n.r.	180 ℃, 507psi H_2 300h,SBP	--/77%/--	n.r.	[40]

(Note: PZ-Particle size-, DI- dry impregnation, Conv.-Conversion, Sel.-Selectivity, Com.-Commercial, Immo.-Immobilization, n.p.-non-reported and rates are obtained from ref.14.)

Table 1.2 Summary of Ru nanoparticle preparation.

Support	Metal	Metal wt%	Method	PZ (nm)	Precursor	Ref.
Active Carbon	Ru	5	WI	6.0	$RuCl_3$	[41]
Active Carbon	Ru	2	DI	3.9[a]	$RuCl_3$	[42]
Active Carbon	Ru	1	DI	6.0	$RuCl_3$	[43]
Active Carbon	Ru	2	DI	7.4	$RuCl_3$	
Active Carbon	Ru	5	DI	10.6	$RuCl_3$	
Active Carbon	Ru	10	DI	16.8	$RuCl_3$	
Active Carbon	Ru	5	WI	1.7	$RuCl_3$	[44]
Active Carbon	Ru	1	WI	2.5	$RuCl_3$	[45]
Active Carbon	Ru	3	WI	2.0	$RuCl_3$	
Active Carbon	Ru	5	WI	1.5	$RuCl_3$	
Active Carbon	Ru	1.5	DI	1.5～2.2	$Ru(NO)(NO_3)_3$	[46]
Carbon	Ru	2.0	WI	1.5	$Ru(NO)(NO_3)_3$	[47]
Carbon	Ru	2.0	WI	3.3	$RuCl_3$	[48]

Carbon	Ru	20	WI	1.0～10	$RuCl_3$	[49]
Carbon	Ru	2.0	WI	4.2	$RuCl_3$	[47]
γ-Al_2O_3	Ru	5.0	WI	15.2	$RuCl_3$	[41]
γ-Al_2O_3	Ru	4.0	DI	1.6～2.4	$RuCl_3$	[50]
γ-Al_2O_3	Ru	4.0	WI	0.84	$Ru(NO)(NO_3)_3$	[51]
γ-Al_2O_3	Ru	5.0	WI	10.8	$Ru(NO)(NO_3)_3$	[52]
γ-Al_2O_3	Ru	1.8	WI	1.7～2.3	$Ru(NO)(NO_3)_3$	[53]

Note: WI-wetness impregnation, a- particle size analyzed by H_2-O_2 chemisorption, all others determined by electron microscopy.

Chapter 2. Experimental Design

2.1 Characterization Methods

The characterization techniques used in this study are listed in Fig. 2.1.

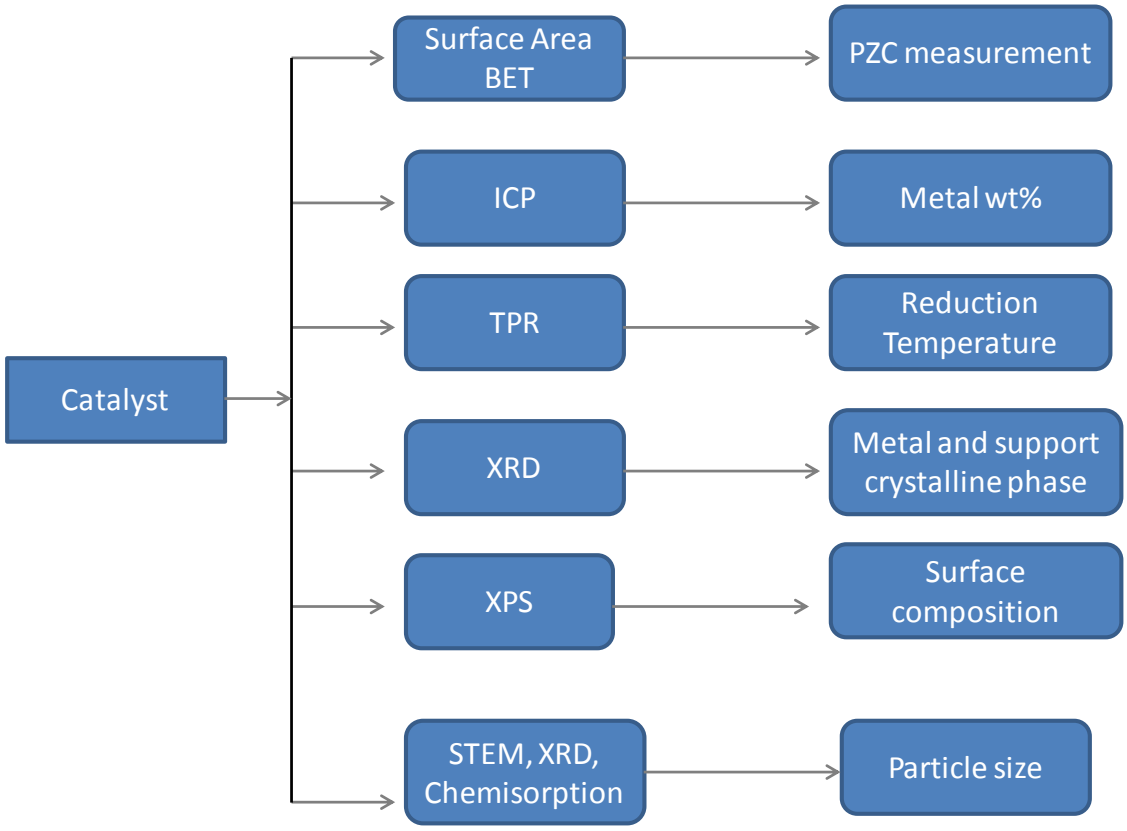

Figure 2.1 Schematic diagram of catalysts characterization.

2.1.1 BET surface area

BET surface area was measured using a Micromeritics ASAP 2020 system. The samples were first degassed at 110^{o}C and 10^{-3} Pa. Then nitrogen was charged on the samples across a wide range of relative pressures at 77 K. This technique provides information about the type of isotherm, surface area and pore size distribution of the samples analyzed. The BET specific surface area was evaluated using the linear relation between P/P_0 and $1/ [v/ (P/P_0-1)]$ with 8 points from 0-0.35 of P/P_0 values.[54-56]

2.1.2 Inductively coupled plasma-atomic emission spectrometry (ICP-AES)

ICP-AES was performed using PerkinElmer. This is one of the most common techniques for elemental analysis. This technique is based on the measurement of the emission at one wavelength, which is highly selective for a specific element. The schematic diagram of a typical ICP-AES set-up is shown in Fig. 2.2. When an aqueous sample solution is introduced into the spectrometer, it becomes atomized into a mist-like cloud. This mist is carried into the argon plasma with a stream of argon gas. The plasma (ionized argon) produces temperatures close to 7000 ℃, which thermally excites and emits light wavelengths characteristic of its elements. A mirror reflects the light through the entrance slit of the spectrometer onto a grating that separates the element wavelengths onto photomultiplier detectors.[57]

2.1.3 Temperature Programmed Reduction (TPR)

TPR is widely used technique for the characterization of metal oxides dispersed on a support. By this method, quantitative information of the reducibility of the oxide's

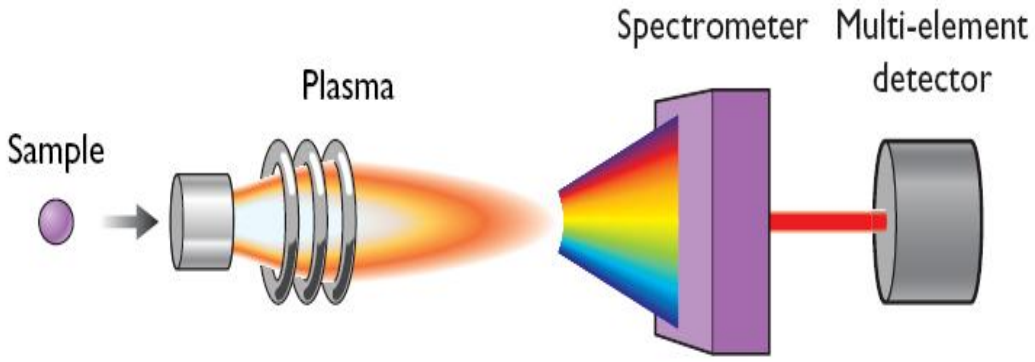

Figure 2.2 Schematic set-up of ICP-AES.[57]

surface and the heterogeneity of the reducible surface can be provided, which is very helpful to find the most efficient reduction conditions. For this study, TPR experiments were performed in a [name of the TPR equipment, manufacturer CHEBET 3000. First a reducing agent preferably a mixed gas of 10% hydrogen diluted in argon was applied on the sample while sample temperature was being increased linearly with time. A thermal conductivity detector (TCD) was applied to measure changes in the thermal conductivity of the gas stream with temperature.[54, 58, 59] If hydrogen is consumed, it could be easier to detect by TCD because hydrogen has the highest thermal conductivity among the common gases, the thermal conductivity of some common gases at 25℃ has been summarized in Table 2.1.[60]

Table 2.1 Thermal conductivity of some common gases at 250 ℃.

Species	Thermal Conductivity W/(m*K)
Nitrogen	0.0240
Hydrogen	0.1680
Oxygen	0.0266
Argon	0.0160
Carbon dioxide	0.0146
water	0.5800

2.1.4 X-Ray Diffraction (XRD)

XRD is primarily used for phase identification of a crystalline material and can provide unit cell information. X-rays are generated by a cathode ray tube, which is filtered to produce monochromatic radiation and then directed toward the sample. The interaction of the incident rays with sample produces constructive interference when the conditions satisfy the Bragg's law.

$$n\lambda = 2d \sin\theta \tag{2-1}$$

where n is an integer, Θ is the wavelength of incident wave, d is the spacing between the planes in the atomic lattice and Θ is the angle between the incident ray and the scattering plane. These diffracted X-rays are detected, processed and counted. All possible diffraction directions of the lattice were obtained after scanning the sample through a range of 2Θ angle.

XRD is a bulk technique, which is suited for identification of crystal structure of an unknown material and measurement of the average particle size. However, this method does have some limitations. Firstly, the large amount of sample is required for XRD experiment. Secondly, if the particle size is less than 2nm, it will not be identified

by the detector. In general, the larger the particle is, the sharper intensity signal is. Lastly, if the metal weight loading is less than 1%, XRD may not be able to detect that metal . X-ray diffraction (XRD) analysis for all catalysts was performed using a Rigaku MiniFlex II bench top system at 2θ=10°C-80 ℃. The XRD patterns were compared to JCPDS reference spectra using PDXL software. The radiation source was Cu Kα (λ=1.5405 Å) at operating conditions of tube voltage of 30 KV and a current of 15mA. All spectra were taken at a scan rate of 0.5 °/min and a sampling width of 0.02°. According to the XRD pattern, the particle size was calculated from the Scherrer Equation.

$$d = K\lambda / B\cos\Theta \tag{2-2}$$

where d is the average crystal particle diameter, K is a constant (usually between 0.9-1), λ is the X-ray wavelength, B is the width in radians at half the maximum intensity of the peak and Θ_B is the position of the peak at maximum intensity.[54, 58, 61]

2.1.5 Scanning Transmission Electron Microscopy (STEM)

STEM is a powerful technique for viewing metal particles deposited on the support. Scanning transmission electron microscopy (STEM) was used to image the materials with a JEOL 2100F 200kV FEG-STEM/TEM equipped with a CEOS C_s corrector on the illumination system. The geometrical aberrations were measured and controlled to provide less than a π/4 phase shift of the incoming electron wave over the probe-defining aperture of 17.5 mrad. High angle annular dark-field (HAADF) STEM images were acquired on a Fischione Model 3000 HAADF detector with a camera length such that the inner cut-off angle of the detector was 50 mrad. The scanning acquisition was synchronized to the 60 Hz AC electrical power to minimize 60Hz noise in the images and a pixel dwell time of 15.8 μs was used.[54, 58]

2.1.6 H_2-chemisprotion

Chemisorption refers to the chemical adsorption and desorption phenomena by which gas or vapor molecules bond to or are released from the solid surface of sample materials. The method is the most sensitive to count metal surface atoms because all surface atoms are independent of crystallite size and probed at the molecular level. In addition, since the strong chemisorption is irreversible on the reduced metal surface, it is widely applied for support catalysts, especially when a significant fraction of small particles (less than 2 nm) are present which are difficult to detect by XRD. In this method, firstly, the surface of the catalyst was cleaned and reduced to metallic state, which was treated at proper temperature with flowing H_2 and then exposed to O_2 in order to cover the metal surface with oxygen at room temperature. Finally, H_2 was used to titrate the precovered oxygen atoms at proper temperature. Since the amount of consumed H_2 is known, the amount of oxygen atom covered on the metal surface and the number of metal atoms on the surface can be determined by the adsorption stoichiometry. [58, 62]

2.1.7 X-Ray Photoelectron Spectroscopy (XPS)

XPS is a surface sensitive technique that is used to obtain the chemical information about the surfaces of solid materials, such as the elemental composition and the chemical state of surface component. The peak position and peak area obtained from XPS are used to evaluate the composition, while the peak shape provides the information about chemical shifts or chemical bonds of the elements. XPS measurements were conducted using a Kratos AXIS Ultra DLD XPS system equipped with a monochromatic Al K source. The energy scale of the system is calibrated using a Au foil with Au4f

scanned for the Al radiation and a Cu foil with Cu2p scanned for Mg radiation resulting in a difference of 1081.70 ± 0.025 eV between these two peaks. The binding energy is calibrated using an Ag foil with $Ag3d_{5/2}$ set at 368.21 ± 0.025 eV for the monochromatic Al X-ray source. The monochromatic Al K source was operated at 15 keV and 120 W. The pass energy was fixed at 40 eV for the detailed scans. A charge neutralizer (CN) was used to compensate for the surface charge.[54, 58]

2.1.8 Gas Chromatography (GC)

GC is a method for separating the components of a solution that can be vaporized without decomposition to measure their relative quantities. Typically, this technique is used for purification and reaction solution analysis. In a typical GC operation system presented in Fig. 2.3, an inert carrier gas (typically, helium or nitrogen) carries the vaporized compounds through a column at different rates depending on their various chemical and physical properties and their interaction with the walls of the stationary column. Sample components are separated based on their boiling points and relative affinity for the stationary phase, which is most often a viscous liquid within the column. The higher a component's affinity for the stationary phase, the slower it comes off the column. This causes each compound to elute at a different time, known as the *retention time* of the compound which is then detected and identified electronically and represented as peaks on a chromatogram. Other parameters that can be used to alter the order or time of retention are the carrier gas flow rate, column length and the temperature.[63]

The precision of repeated injections in GC is not particularly good, either by auto sampler injection or manual injection, certainly worse than the loop injectors used in HPLC. Therefore, internal standard is primarily used to improve the accuracy and

precision of quantitative analysis that have large inherent variability. In general, an internal standard is a known concentration of a substance that is present in every sample

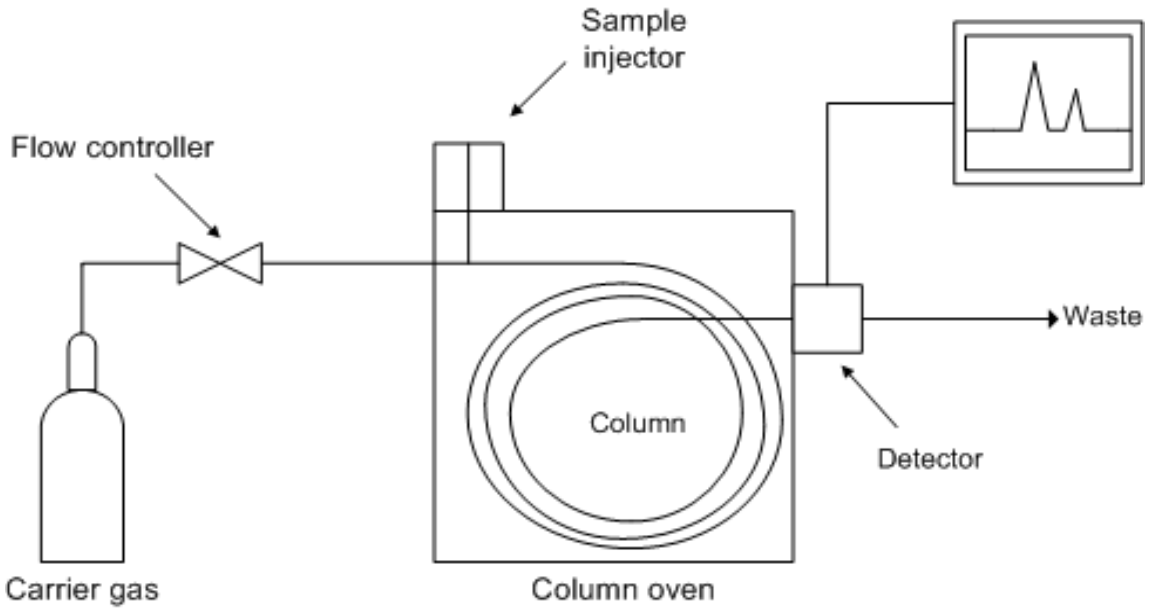

Figure 2.3 Schematic diagram of gas chromatography.

analyzed. A compound similar to the analyte of interest is added to the sample and run. By having the analyte and the standard elute in the same run, the run to run variability is eliminated giving more precise results ,where the internal standard is to behave similarly to the analyte but to provide a signal that can be distinguished from that of the analyte. Ideally, any factor that affects the analyte signal will also affect the signal of the internal standard to the same degree. Thus, the ratio of the two signals will exhibit less variability than the analyte signal.[64]

2.2 Materials

Hexaammineruthenium(III) chloride ($Ru(NH_3)_6Cl_3$), Potassium hexacyanoruthenate(II) hydrate $K_4Ru(CN)_6$), Levulinic acid (98%), 1,4 Dioxane (99.8%) and Potassium nitrate (>99.9%) were purchased from Sigma-Aldrich. While 5% Ru on

activated carbon and 5% Ru Al_2O_3 commercial catalysts were obtained from Strem Chemicals. Vulcan XC 72 (Surface area is 250m^2/g, PZC ~8.2) and SBA-200-gamma-Alumina (Surface area is 189m^2/g, PZC ~8.3) supports were obtained from Cabot and Aerosil, respectively.

2.3 Ruthenium based catalyst preparation

2.3.1 Oxidized carbon synthesis

A commercial carbon (Vulcan XC72) was used as the starting material for oxidized VXC72. 10g of VXC72 support mixed with concentrated nitric acid (>70%) was heated for 3h at its boiling temperature 90-95℃ and then cooled down to room temperature. Subsequently, the mixture was washed with deionized water until the pH of the washing solutions reached 5 and was dried overnight at room temperature. Prior to catalyst synthesis, the sample was calcined for 1h at 300℃ in order to release a great number of micropores, from which surface oxygen groups are not removed.[26, 29] The oxidized Vulcan 72 Carbon is labeled as Cox.

2.3.2 Control pH shift experiment (metal free)

A control pH shift experiment was performed at 1000 m^2/l surface loading. It should be noted that the same loading was used later to synthesize catalysts via SEA. At first, a series of 50ml solution with incremental pH values from 1-13 (adjusted by adding HCl or HNO_3 to DI water) was prepared and placed in 60-ml polypropylene bottles. Afterwards fixed amount of support powder w weighed out and added to the solution to achieve the desired surface loading of 1000 m^2/l and then shaken for 1hour after which the final pH was measured. It has been reported that it is enough to reach adsorption

equilibrium.[23, 32] PH measurements were conducted with a general combination pH electrode. The initial pH (pH_i) vs. final pH (pH_f) values were plotted.[30]

2.3.3 Determination of the optimal adsorption pH

In order to determine the pH at which maximum metal uptake could be achieved, adsorption experiments were conducted at a specific range of pH values (selected based on the PZC of the support). The process is quite similar to the control pH shift experiment. At first stock solution of metal precursor solution (e.g., Ru $(NH_3)_6Cl_3$) of specific concentration was prepared and aged for 1 hour. After that a series of 50-ml pH adjusted (using HCl or NaOH) solution with desired metal concentration was prepared from the stock and then placed in 60-ml polypropylene bottles. For cationic precursors adsorption was studied within the pH range range of 9-13 whereas for anionic the range was 1-6 where electrostatic attraction is dominant. After final pH measurements 5-ml from each solution was filtered using 0.2 micro syringe filters for ICP measurement to determine the final metal concentration. Additionally, prior to adding support 5-ml from each solution was also extracted and stored separately for ICP analysis to determine the initial metal concentration (before support addition). Difference between initial and final metal concentration for each pH sample solution is referred to as the adsorbed metal at that pH all of which were then plotted against the final pH values. From this plot the final pH value at which maximum uptake was observed was noted as the optimum pH.

2.3.4 Synthesis of Ru based catalysts

2g of 1.5% Ru/Cox and 2% Ru Al_2O_3 catalysts were prepared with 100ppm Ru $(NH_3)_6Cl_3$ at SL=1000m^2/l at optimal initial PH ～ 11.6 and 100ppm $K_4Ru(CN)_6$ at SL=500m^2/l at optimal initial PH ～1.95, respectively. 4.4% Ru Cox catalysts were also

prepared by performing sequential SEA 3 times at the same condition as 1.5% Ru Cox $_{SEA}$ catalyst. Afterwards, the catalysts were dried in room temperature for 48h, and then at 100◦Covernight. For comparison, the same amounts of Ru metal loading catalysts were prepared by dry impregnation (DI) or pore filling. The amount of liquid used for DI was equal to the pore volume of the support and was not pH-adjusted (only deionized water). The concentrations of Ru solution were adjusted to obtain desired weight of metal. Dry impregnation was also used to dope the same amount of Potassium (KNO_3) in 2% Ru γ-Al_2O_3 prepared by DI sample into 1.5% Ru Cox and 2% Ru γ-Al_2O_3 both prepared by SEA catalysts.

2.4 Catalyst Characterization

Surface areas of Cox and γ-Al2O3 were obtained by nitrogen adsorption-desorption isotherms measurement with a Micromeritics 2020 ASAP instrument. This experiment was carried out at 77K after degas at 10^{-3} Pa for 8h at 110 ℃. The concentration of Ru in the solution was determined by inductively coupled plasma-atomic emission spectrometry (ICP-AES). Temperature programmed reduction (TPR) experiment of all prepared Ru catalysts were performed on a ChemBET 3000 station (Quantachrome Instruments). Typically, a certain amount of dried, unreduced catalyst sample was loaded into a conventional U-tube reactor positioned in a furnace equipped with a temperature controller. The sample was exposed to the 20 ml/min flow of 5 % H_2/N_2 while the temperature was ramped at 10 ℃/min to 800 ℃. A thermal conductivity detector was used to monitor the H_2 concentration in the flow as a function of temperature and the data were recorded using the TPRWin software. To examine the lattice structures of the Ru and support as well as calculate Ru particle size, X-ray

diffraction (XRD) analysis was performed using a Rigaku MiniFlex II bench top system at 2θ=10°C-80 ℃. The XRD patterns were compared to JCPDS reference spectra using JADE software. The radiation source was Cu Kα (λ=1.5405 Å) at operating conditions of tube voltage of 30 KV and a current of 15mA. All spectra were taken at a scan rate of 0.5 ℃/min and a sampling width of 0.02°. The Ru metal particle size also was measured by scanning transmission electron microscopy (STEM) and hydrogen chemisorption. STEM was performed on the reduced catalyst samples and carried out by using a JEOL -2100 F microscope equipped with a field emission electron gun source and operated at 200kV and with an extracting voltage of 4.5KV. Around 1000 Ru particles were used for the particle size analysis in order to obtain the particle size distribution and the mean particle size. Chemisorption was performed by hydrogen titrating oxygen of precovered Ru on a Micromeritics AutoChem II 2920 automated Chemisorption Analyzer to determine the concentration of Ru active sites on the surface. Approximately 0.1g reduced catalyst was pretreated in flowing 10% H_2 at 300◦C for 3h, then exposed to 100% Ar flow for 1h at 300 ◦C in order to remove chemisorbed hydrogen from the metal surface. Following this, sample was cooling to 40◦C in flowing Ar, then exposed to 10% O_2/Ar for 30mins to absorb atomic oxygen on Ru surface. Subsequently, 100% Ar was passed through to remove residual O_2 in order to make sample ready for H_2 titration. H_2 titration occurred at 250◦C with purging10% H_2/Ar, the adsorbed atomic oxygen rapidly with H_2 to form water and replace one adsorbed oxygen atom with an atomic hydrogen atom. A calibrated, high sensitivity thermal conductivity detector was quantitatively determined the H_2 consumption. To check the charge of Ru on the surface, XPS measurements were conducted using a Kratos AXIS Ultra DLD XPS system equipped with a monochromatic

Al K source. The monochromatic Al Ksource was operated at 15 keV and 120 W. The samples were analyzed under identical conditions and the resulting spectra were fitted by applying a Shirley-type background subtraction and a charging correction with reference to Carbon 1s at 284.5 eV.

2.5 Catalytic experiments: Levulinic Acid (LA) Hydrogenation

The hydrogenations of LA reactions were performed in a 100ml capacity autoclave reactor (Parr Instruments Co.USA) with the stirring speed of 1000 rpm. The typical reaction condition was: H_2 pressure 200psi, temperature 220 ℃ for 6h. Because Ru based catalysts are active for this reaction and the high conversion of LA can be obtained, if too much catalyst was used, the reaction rate could not be calculated. To solve this problem, small amount of Ru catalyst was loaded in the reactor. In the catalytic test, the information of all as-prepared Ru catalysts has been listed in the table 2.2. 1,4 Dioxane was used as solvent because of its non-polar property. At first catalysts were reduced in the mixture of 54g 1,4 dioxane and 200μl diglyme (internal standard) with flowing H_2 at 220 ℃ for 1h. After 1h, the reactor is pressurized with H_2 to the total pressure 422psi (the partial vapor pressure of 1,4 Dioxane at 220 ℃ is 222psi, thus the pressure hydrogen is 200psi), then 3g LA was pumped into the reactor with high pressure HPLC pump (PERKIN ELMER MODEL 250 BINAEY LC PUMP). Liquid samples were taken periodically. Sample taken during the reaction were analyzed by the 5890 series GC system coupled with FID deteror operating at 220 ℃ and caplillary column (RTX-5 capillary column 30 m lengths, 0.25mm id). A carrier gas (He) flow was 1.7 ml/min and the following temperature programme methods was used for GC analysis: 40 ℃ (4min)- 8 ℃/ min-120 ℃ (4min).The injector temperature was also 220 ℃.

Table 2.2 All Ru catalysts used for catalytic evaluation and Ru particle size analyzed by STEM and H_2-O_2 titration chemisorptions.

Catalyst	Particle size/nm	
	STEM	H_2-O_2 titration chemisorption
1.5% Ru Cox $_{SEA}$	1.3	3.8
4.4% Ru Cox $_{3\ times\ sequential\ SEA}$	1.5	4.5
1.5% Ru Cox $_{DI}$	2.1	7.7
5% Ru AC $_{commercial}$	2.5	6.2
2% Ru γ- $Al_2O_{3\ SEA}$	0.9	1.7
2% Ru γ- $Al_2O_{3\ DI}$	1.3	2.5
5% Ru γ- $Al_2O_{3\ commercial}$	4.8	5.5
1.5% Ru Cox $_{SEA\ doped\ K+}$	1.3	4.6
2% Ru γ- $Al_2O_{3\ SEA\ doped\ K+}$	0.9	1.6

2.6 Stability test of the Ruthenium based catalysts

To check whether the Ru particle sinter after reaction, the stability test of all used Ru catalysts were performed by XRD. Due to the large amount of catalysts requested by XRD experiment, 0.5g catalyst was tested in the same reaction conditions, after 6hs, catalysts were filtrated and dried overnight at ambient temperature before XRD.

Chapter 3. Results and Discussion

3.1 Metal (Ruthenium) uptake survey on Carbon and γ-Al_2O_3

The pH shift plots for the determination of PZCs of VXC-72 and γ-Al_2O_3 are shown in Fig 3.1. This experiment was performed at very high surface loading: SL=60000 m^2/l for VXC72 and SL=50000 m^2/l for γ-Al_2O_3 respectively. These curves clearly show a plateau for both types of support corresponding to the PZC value which was 8.6 in the case of VXC72 and 8.2 when the support was γ-Al_2O_3. As explained in the introduction, due to the particularity of the surface functional group of carbon, the PZC of carbon can vary from high value to low value by changing the surface functional group as is the case with oxidized carbon. The PZC of oxidized carbon was also determined with SL=1000 m^2/L (shown in a later figure, Fig 3.3b) and the PZC value obtained was 4.

The next step was to find a stable precursor in the acidic or basic pH range. In the market, only few Ru precursors can be found. For precursors containing anionic Ru complexes, there is $K_4Ru(CN)_6$ and $(NH_4)_2RuCl_6$. There is also $Ru(NH_3)_6Cl_3$ which has a cationic Ru metal complex. Prior experiments have shown however that $(NH_4)_2\,RuCl_6$ is not stable because precipitation can be observed at the acidic pH range. When SEA is applied, anionic Ru metal complex can be used for the support with high PZC and cationic Ru metal complex for the support with low PZC. The purpose was to make Ru catalysts supported on carbon and γ-Al_2O_3. Initially, Ru uptake survey was done with $Ru(CN)_6^{4-}$and VXC-72. The Ru uptake curves are shown in Fig 3.2, where poor uptake was observed. This may have been due to organic vapors in air adsorbed on

the surface sites of the carbon that was used, which was obtained from old stock. Adsorbed organic substances could have blocked these sites resulting in a retarded metal complex adsorption during SEA experiments. In order to test this hypothesis, VXC 72 was calcined at 300℃ for 3hrs to attempt removing any volatile adsorbate. The uptake experiment was performed again, this time on the calcined sample. However, poor uptake was still observed. The reason for the poor affinity of VXC 72 for $Ru(CN)_6^{4-}$ complex is unkown.

The Ru uptake curves and pH shifts of control and adsorption experiments are shown in Fig.3.3 a and b respectively. The plot in Fig.3a shows the final pH value of slurries, after 1h shaking, against Ru surface density, which is defined as the amount of Ru (in μmol) per unit surface area (in m^2) of the support. In this curve, a volcano shaped peak was observed when the final pH value was ~ 9.90, which corresponds to an initial pH value of 11.55 for the Ru $(NH_3)_6Cl_3$ solution shown in Fig.4.3 b. With the same surface loading employed, the metal-containing pH shifts are identical to the metal free control experiment, which can be interpreted by the stability of Ru $(NH_3)_6$ 3+ complex and the independence of adsorption and proton transfer. At the optimal final pH of 9.90, where there was maximum Ru cationic precursor adsorbed on oxidized carbon, the Ru surface density was ~ 0.88 μmol/m^2. This uptake corresponds to an Ru weight loading, defined as the mass of Ru per total mass of the catalyst, of about 1.5% ~ 1.6%.

For the γ-Al_2O_3 support, Fig.3.4 a shows the Ru anionic precursor uptake. The maximum uptake where Ru surface density is 1.3 μmol/ m^2 was observed when the final pH was 2.12, that corresponds to an initial pH of 1.95. Like that of VXC 72, a similar trend was observed for the pH shift of control experiment and metal adsorption (Fig3.4b).

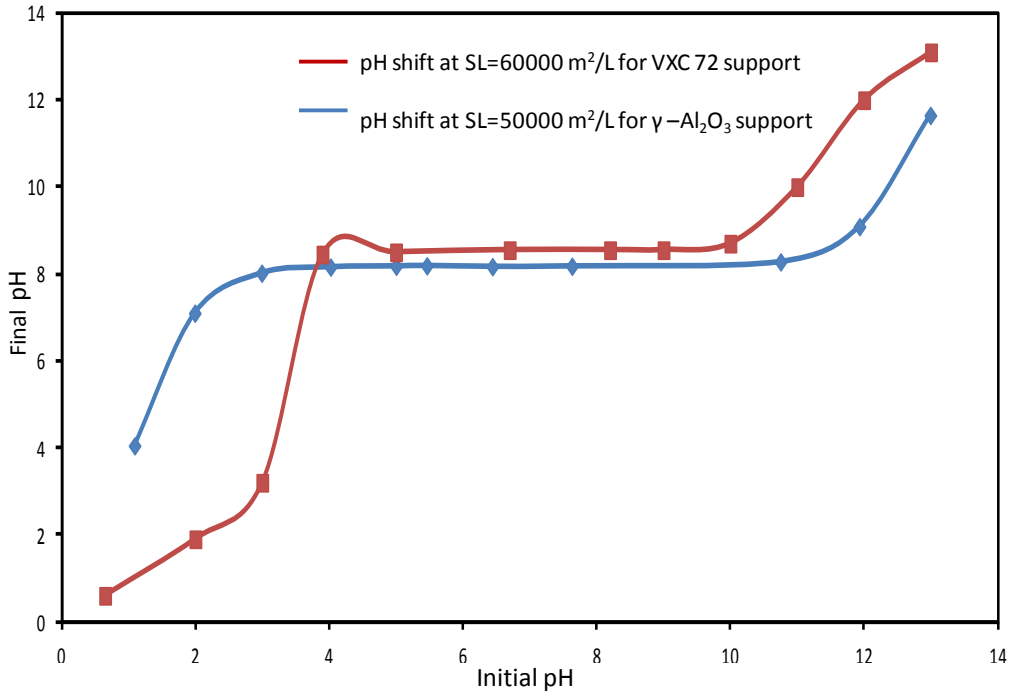

Figure 3.1 PZC determination of VXC 72 at SL=60000m^2/l and γ-Al_2O_3 SL= 50000 m^2/l.

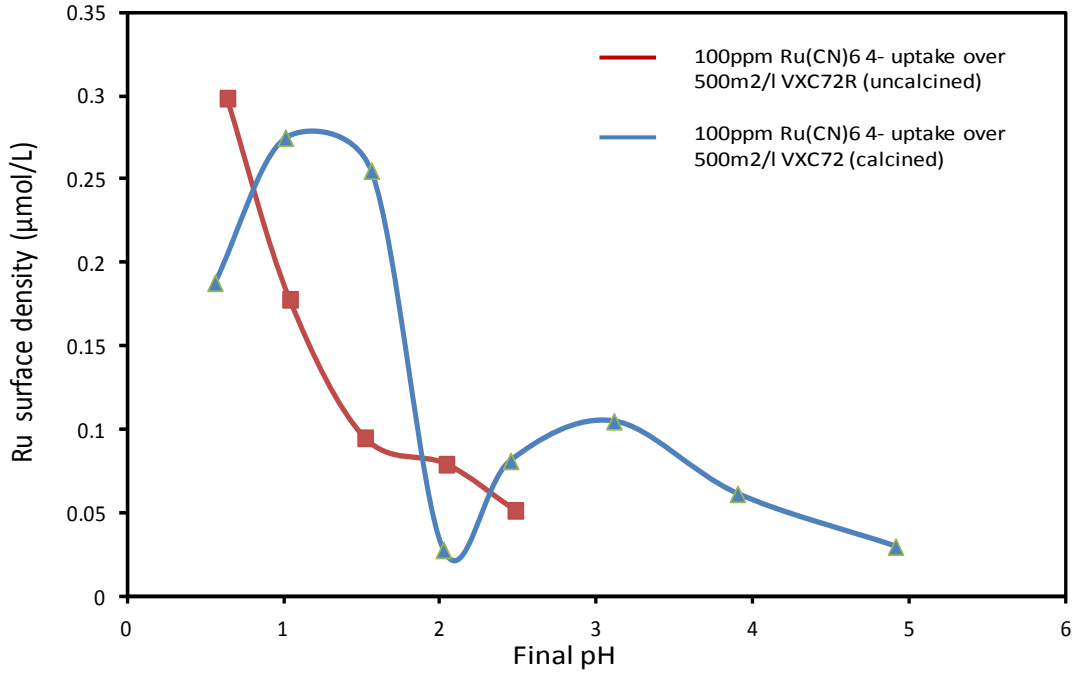

Figure 3.2 Final pH vs. uptake (Γ) plot using 100ppm Ru (from $Ru(CN)_6^{4-}$) solution, on VXC 72 and calcined VXC72 at SL=500 m^2/l.

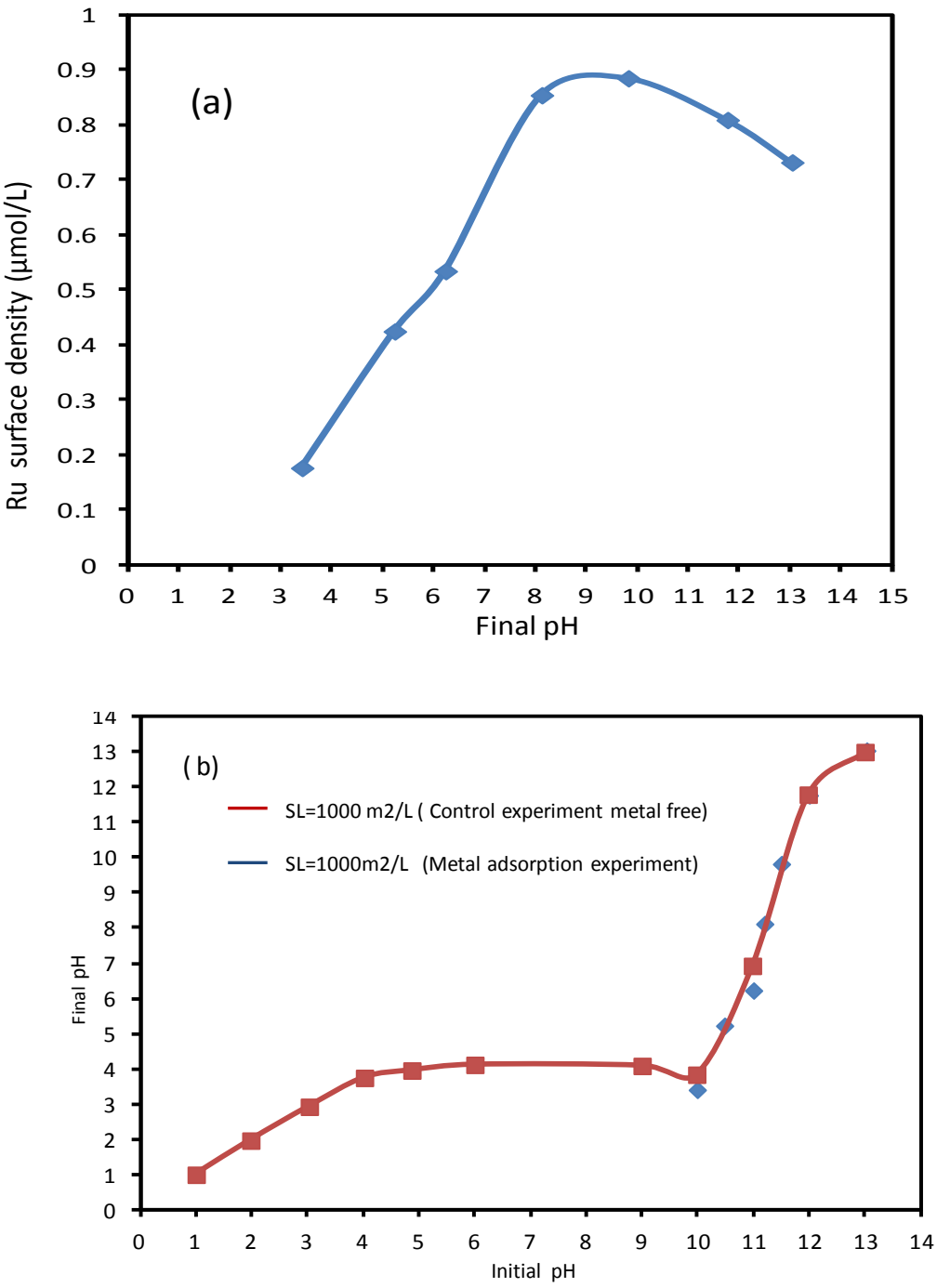

Figure 3.3 (a) Final pH vs. uptake (Γ) plot using 100ppm Ru (from $Ru(NH_3)_6Cl_3$) solution on Cox SL=1000 m^2/l. (b) pH shift of metal free control and adsorption experiments in the same system.

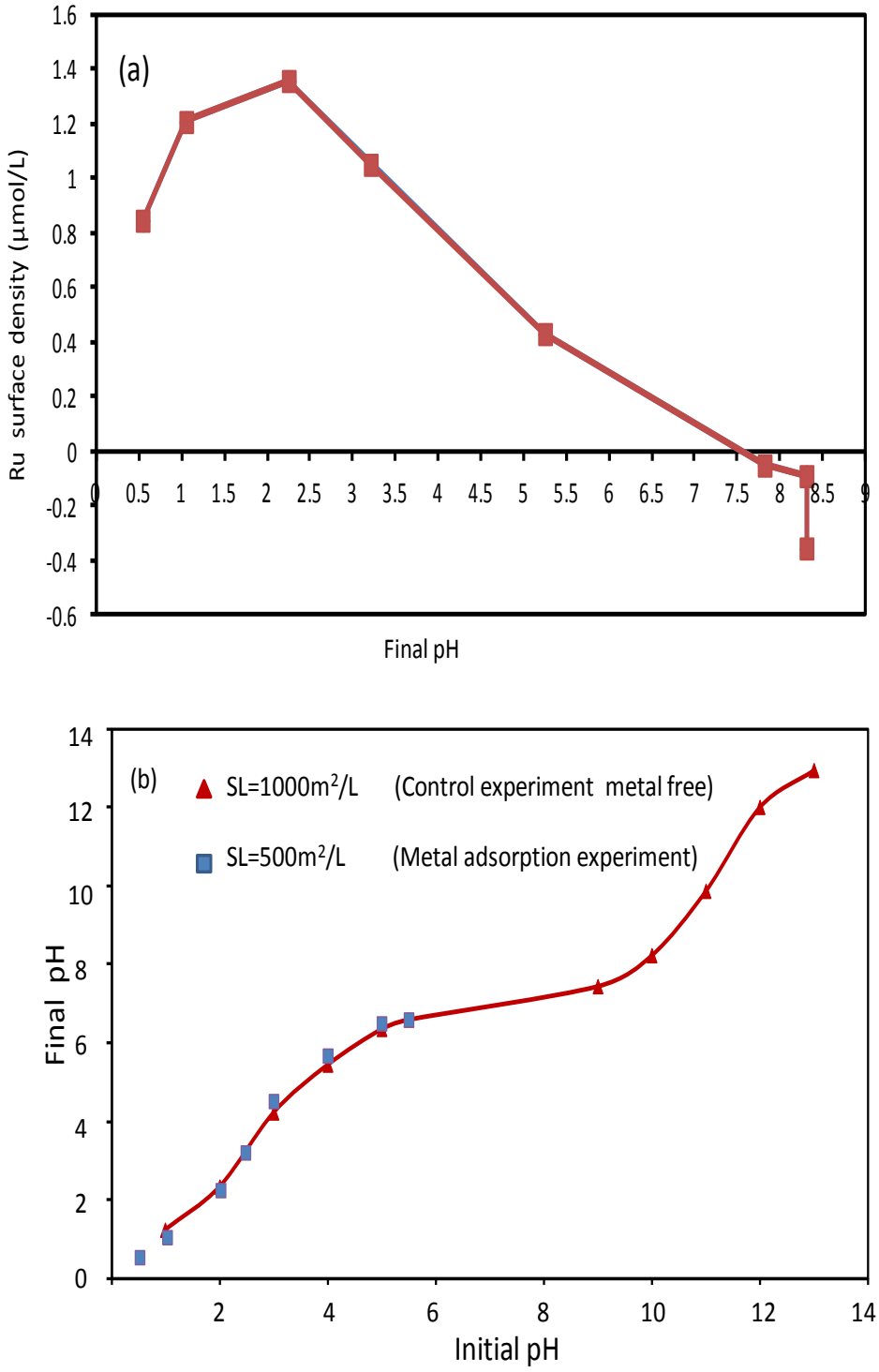

Figure 3.4 (a) Final pH vs. uptake (Γ) plot using 100ppm Ru (from $K_4Ru(CN)_6$) on γ-Al_2O_3 SL=500 m^2/l. (b) pH shifts of metal free control and adsorption experiments in the same system.

3.2 Catalyst synthesis and characterization

3.2.1 Catalyst synthesis

In the Ru uptake survey experiments, only 50ml of Ru precursor was employed, from which only a small amount of the catalysts were obtained, which was not enough since a large amount of catalyst was needed for the characterization and evaluation steps. In order to produce the amount of catalyst required, the SEA system can be scaled up rationally using the results obtained from the Ru uptake survey. In the case of using oxidized carbon support, the uptake survey used 50ml of 100ppm Ru, using $Ru(NH_3)_6Cl_3$, at optimal initial pH ~ 11.6, with enough support added to achieve SL=1000m^2/l. This yielded about 0.2g of catalyst. In order to make around 4g of catalyst, the system was scaled up to use 1L of 100ppm Ru, still from $Ru(NH_3)_6Cl_3$, with its pH adjusted to match the optimal initial pH ~ 11.6. Enough carbon support was added to achieve the same surface loading of 1000m^2/l. Similarly, in producing about 4g of Al_2O_3 supported Ru, the system used 1L of 100ppm Ru, from $K_4Ru(CN)_6$ at an optimal initial pH ~1.95, with enough alumina added to achieve SL=500m^2/l.

3.2.2. H_2- TPR

The TPR patterns of dried, unreduced Ru catalysts are summarized in Fig.3.5. Two obvious peaks were observed for both catalysts in Fig.3.5 a. The lower temperature peak was assigned to the reduction of Ru^{3+} to metallic Ru^0.[24] Another broad peak was assigned to the methanation that occurs at 350 ℃, confirmed by mass spectroscopy results shown in Fig.3.5 b, where H_2 starts to react with carbon support at 350 ℃ resulting in the formation of CH_3^+ (mass 15) fragment and CH_4 (mass 16). For the TPR profile of 1.5% Ru Cox_{SEA}, an additional small peak shows up at 300◦C. It could be explained that the

reduction of this catalyst may have a transition stage, that is, the partial reduction of Ru^{3+} to Ru^{2} takes place at 170 ℃ and then the reduction of Ru^{2+} to metallic Ru^{0} occurs at 300 ℃. Another interesting phenomenon is that a wide H_2 consumption peak is observed in the TPR pattern of the sample prepared by SEA while a sharper and narrower peak is seen in the sample prepared by DI, which are very similar to the TPR profiles of Ru/SiO_2 reported by our group before.[24] In the case of the TPR profile of $Ru/\gamma\text{-}Al_2O_3$ in Fig.3.5 c, only one peak is observed which indicates that Ru^{3+} is directly reduced to metallic Ru. Since about the same amount of Ru metal was used for TPR experiments, the areas of H_2 consumption peaks were about equal for all Ru based catalysts.

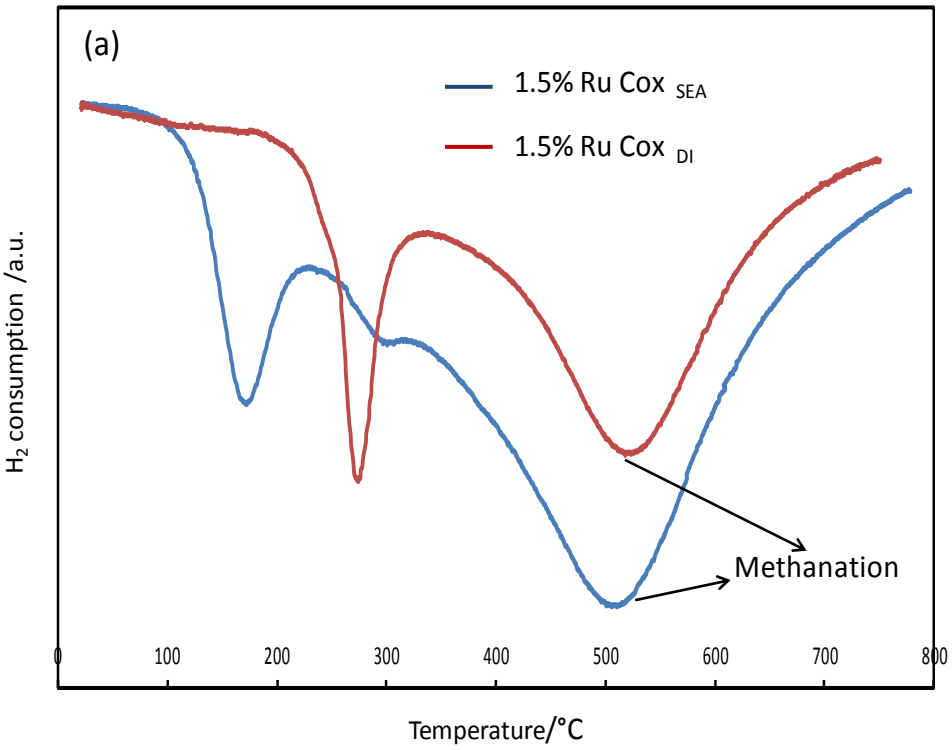

Figure 3.5 (a) H_2-TPR patterns of 1.5% Ru Cox $_{SEA}$ (reduction temp.=250 ℃) and 1.5% Ru Cox $_{DI}$ (reduction temp.=300 ℃).

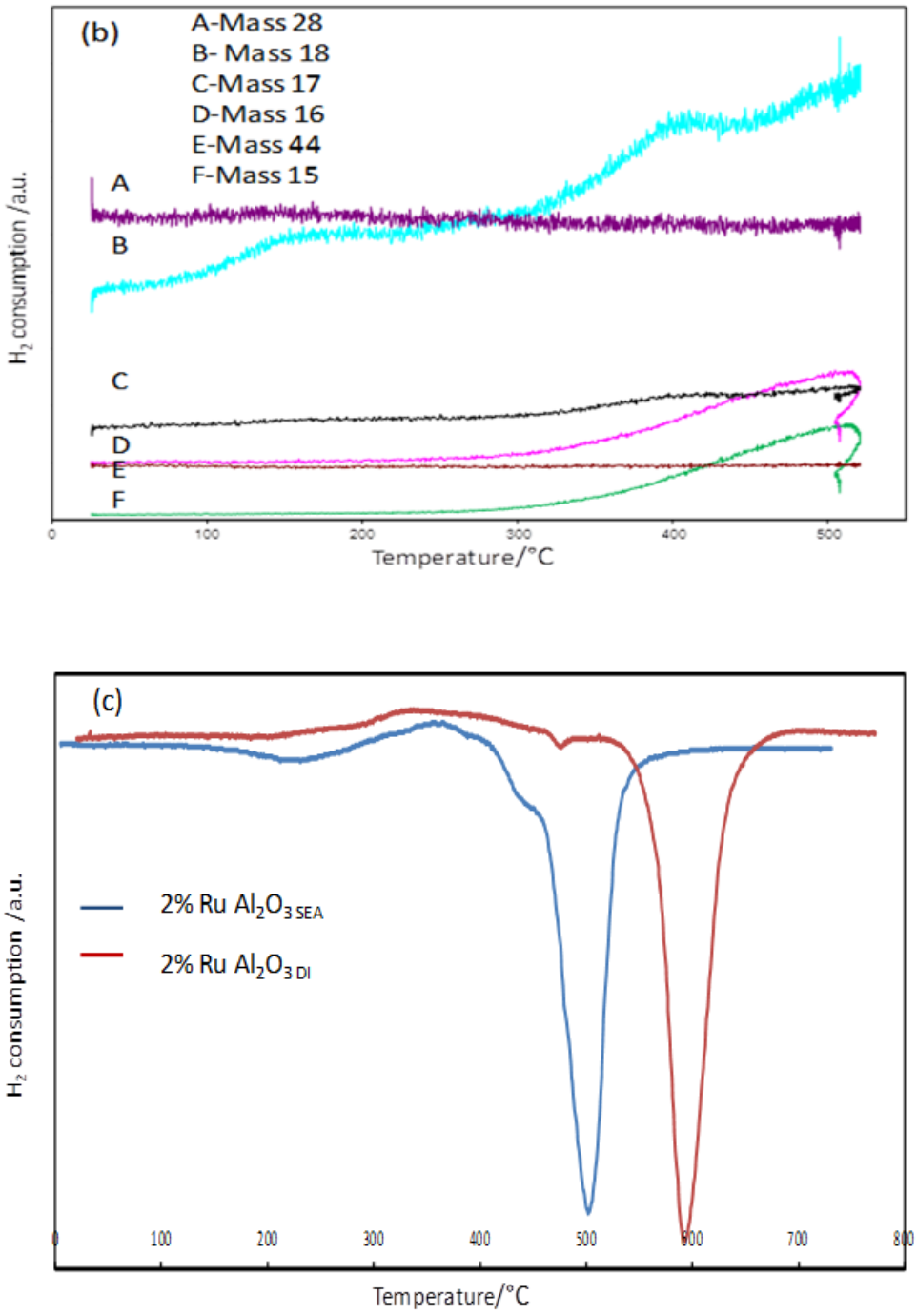

Figure 3.5 (b) H_2-TPR Mass Spectroscopy of 1.5% Ru Cox $_{SEA.}$ (c) H_2-TPR patterns of 2.0% Ru γ-Al_2O_3 $_{SEA}$ (reduction temp.=520 ℃) and 2.0% Ru γ-Al_2O_3 $_{DI}$ (reduction temp.=600 ℃).

3.2.3 XRD

Fig.3.6 a and b show the XRD patterns of Ru catalysts supported on carbon and γ-Al_2O_3 measured under ambient conditions, respectively. In Fig.4.6 a, the diffraction peaks of metallic Ru phase (2θ=38.4°, 42.2°, 44.0°, 58.3° and 69.4°, JCPDS 06-0663)[65] appeared in the XRD patterns of 1.5% Ru Cox_{DI} and 5.0% Ru $AC_{commercial}$. However, the peaks were sharper in the 5.0% Ru $AC_{commercial.,}$ which means larger Ru particles were present in 5.0% Ru $AC_{commercial}$ compared to 1.5% Ru Cox_{DI}. On the other hand, the Ru peaks were not observed for 1.5% Ru Cox_{SEA} catalyst. Due to the limitation of the XRD detector, metal particles less than 1.5nm in size cannot be detected. These indicated that less than 1.5nm average size Ru particles formed in 1.5% Ru Cox_{SEA} catalyst after H_2 reduction treatment and that larger Ru particles formed in 5.0% Ru $AC_{commercial}$ and 1.5% Ru Cox_{DI} catalysts.

In Fig.3.6 b, due to the formation of small Ru particle size in other Ru Al_2O_3 catalysts, the sharp metallic Ru peaks only appear in the XRD pattern of 5% Ru $Al_2O_{3commercial}$ catalyst, where additional peaks located at 2θ=45.66 and 46.02 are seen [66]. These additional peaks correspond to delta Al_2O_3. Thus, the Al_2O_3 support of commercial catalyst is not pure γ-$Al_2O_{3,}$ but a mixture of γ-Al_2O_3 and delta Al_2O_3.

The crystal sizes of metallic Ru on the catalysts were determined by means of the X-ray line broadening method using the Scherer formula and the results are shown in Table 2.2. The sizes obtained from XRD results are in good agreement with STEM data as discussed in a later section.

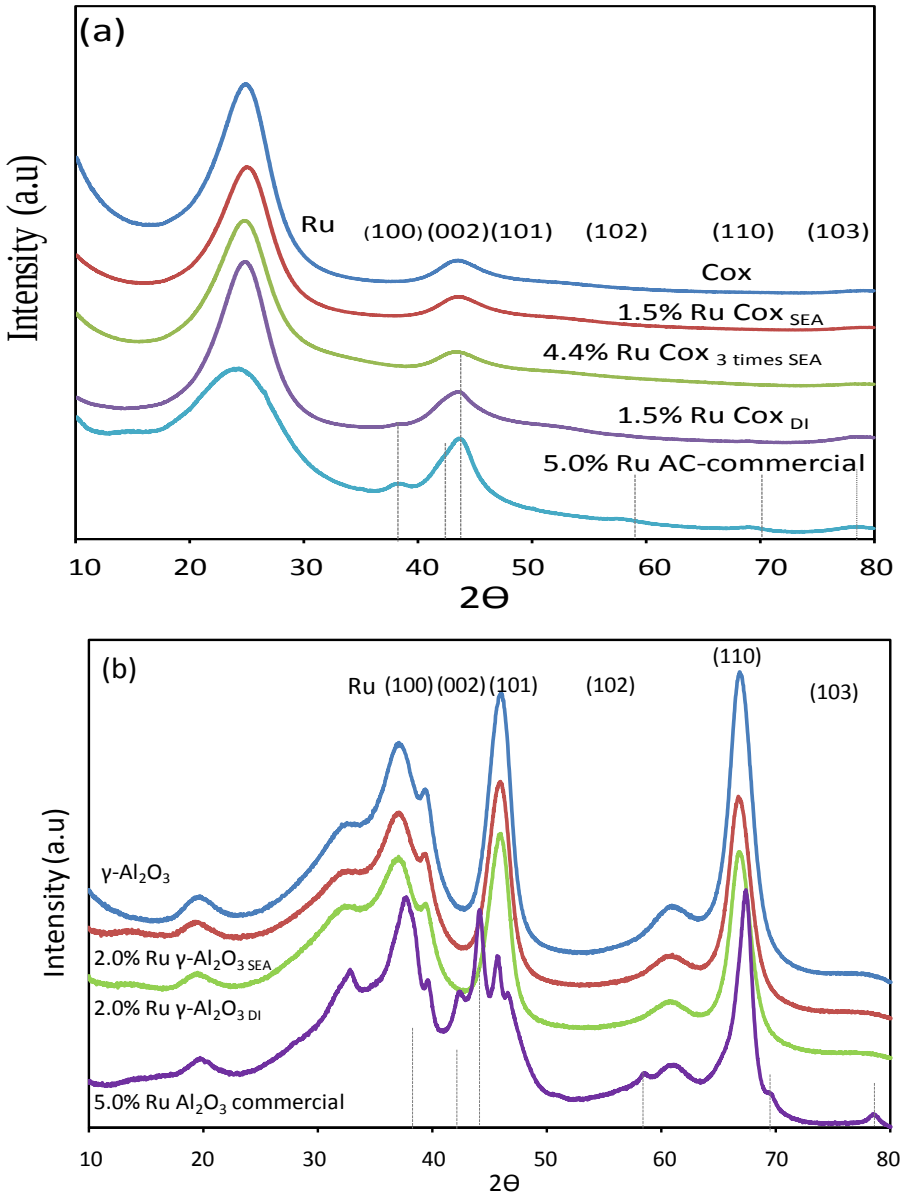

Figure 3.6 (a) XRD results for Ru catalysts supported on Carbon after reduction treatment. (b) XRD results for Ru catalysts supported on Al_2O_3 after reduction treatment.

3.2.4 STEM

Both Fig.3.7 and Fig.3.8 display representative STEM images for all tested catalysts and their corresponding particle size distribution. Ru nanoparticles show up as bright white spots and are seen for all catalysts. From STEM imaging, the average Ru particle diameter (d_{avg}) was calculated from the following equation,

$$davg = \sum_i n_i * d_i^3 / \sum_i nid_i^2 \quad (3\text{-}1)$$

where d_i is the particle diameter measured from the STEM images, assuming hemispherical geometry, and n_i is the number of the particles with that particular diameter [62]. The average Ru particle size varied in this order: In the case of Ru on carbon catalysts, 1.5% Ru Cox $_{SEA}$ (1.3nm) < 4.4% Ru Cox $_{3\text{ times sequential SEA}}$ (1.5nm) < 1.5% Ru Cox $_{DI}$ (2.1nm) < 5% Ru AC $_{commercial}$ (2.5nm). In the case of Ru on Al_2O_3 catalysts, 2.0% Ru γ-Al_2O_{3SEA} (0.9 nm) < 2.0% Ru γ-Al_2O_3 $_{DI}$ (1.3nm) < 5% Ru AC $_{commercial}$ (4.8nm). From all of the particle size analysis results, a common trend found is that very small and well dispersed Ru particles with narrow size distribution were achieved via SEA method.

3.2.5 XPS

The XPS spectra of Ru $3d_{5/2}$---$3d_{3/2}$ for 1.5% Ru Cox $_{SEA}$ are presented in Fig. 3.9 a. Due to the overlapping of the Ru $3d_{3/2}$ peak with the carbon peak (284.5ev), the binding energy of the Ru $3d_{5/2}$ peak was used to determine the oxidation state of Ru present on the surface. For the sample reduced at 250℃ in the XPS vacuum cell, the most intense doublet peaks at 280.2ev and 284.2ev (δ=4.0ev) are attributed to metallic Ru [67]. On the other hand, for the sample reduced at same temperature and then exposed to air, a doublet peak was also observed yet the peak corre sponding to Ru $3d_{5/2}$ is shifted to a higher binding energy of about 280.7ev, which indicates that Ru is oxidized at room

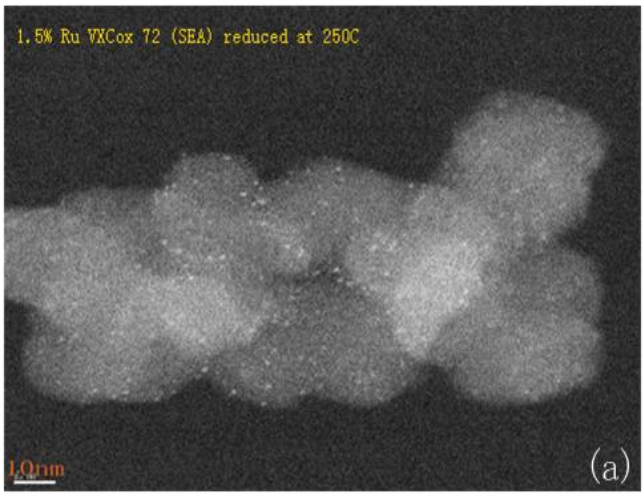
1.5% Ru VXCox 72 (SEA) reduced at 250C
10nm
(a)

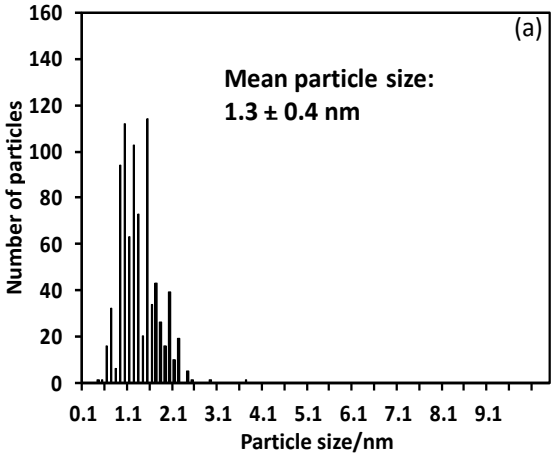
(a)
Mean particle size:
1.3 ± 0.4 nm
Number of particles
Particle size/nm

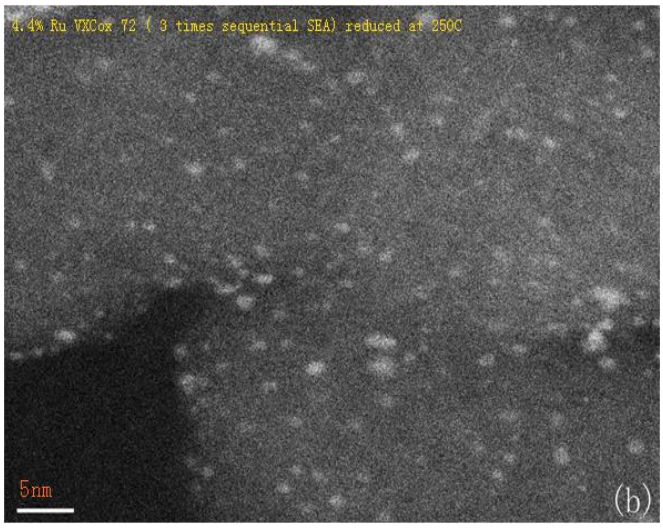
4.4% Ru VXCox 72 (3 times sequential SEA) reduced at 250C
5nm
(b)

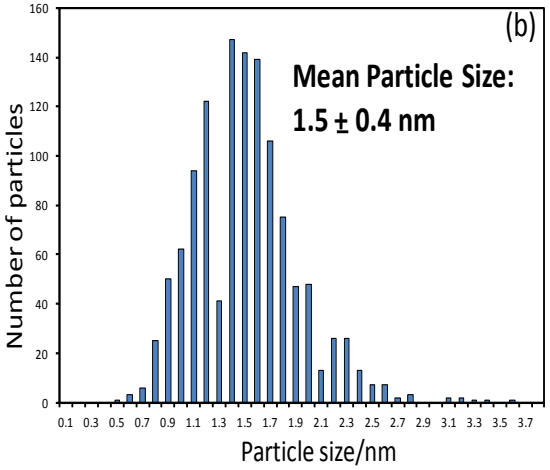
(b)
Mean Particle Size:
1.5 ± 0.4 nm
Number of particles
Particle size/nm

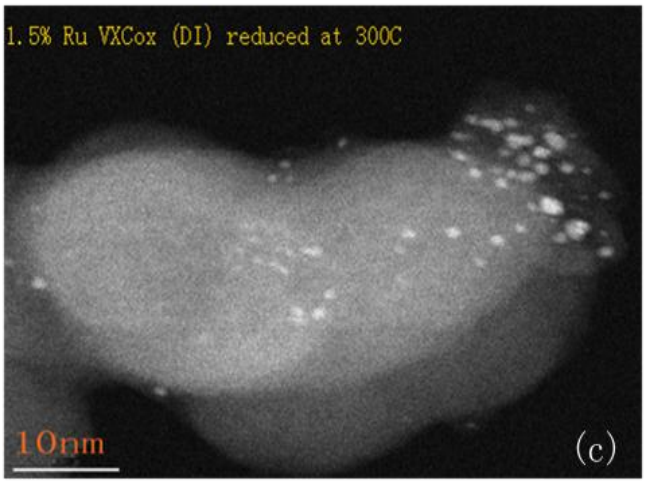
1.5% Ru VXCox (DI) reduced at 300C
10nm
(c)

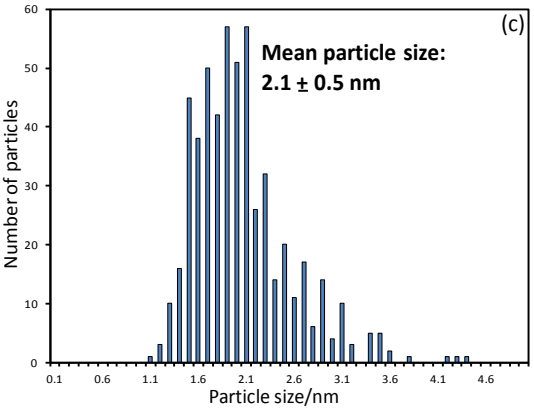
(c)
Mean particle size:
2.1 ± 0.5 nm
Number of particles
Particle size/nm

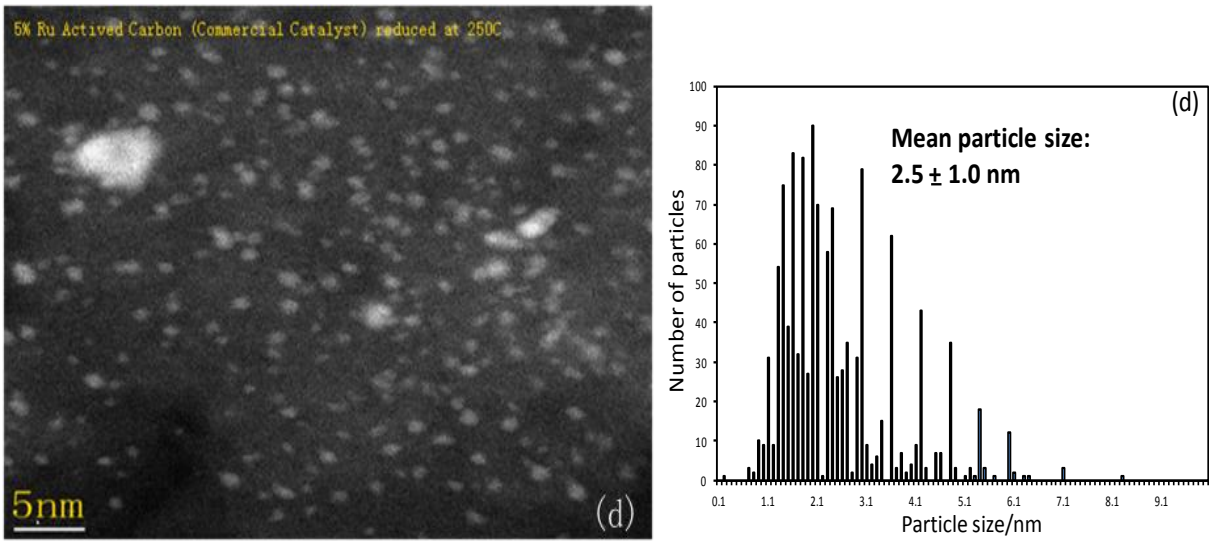

Figure 3.7 Representative STEM images and particle size distributions for Ru catalysts supported on Carbon after reduction treatment. (a)1.5% Ru Cox $_{SEA}$, (b)4.4% Ru Cox $_{3\ times\ sequential\ SEA}$, (c) 1.5% Ru Cox $_{DI}$ and (d) 5.5% Ru AC $_{commercial.}$

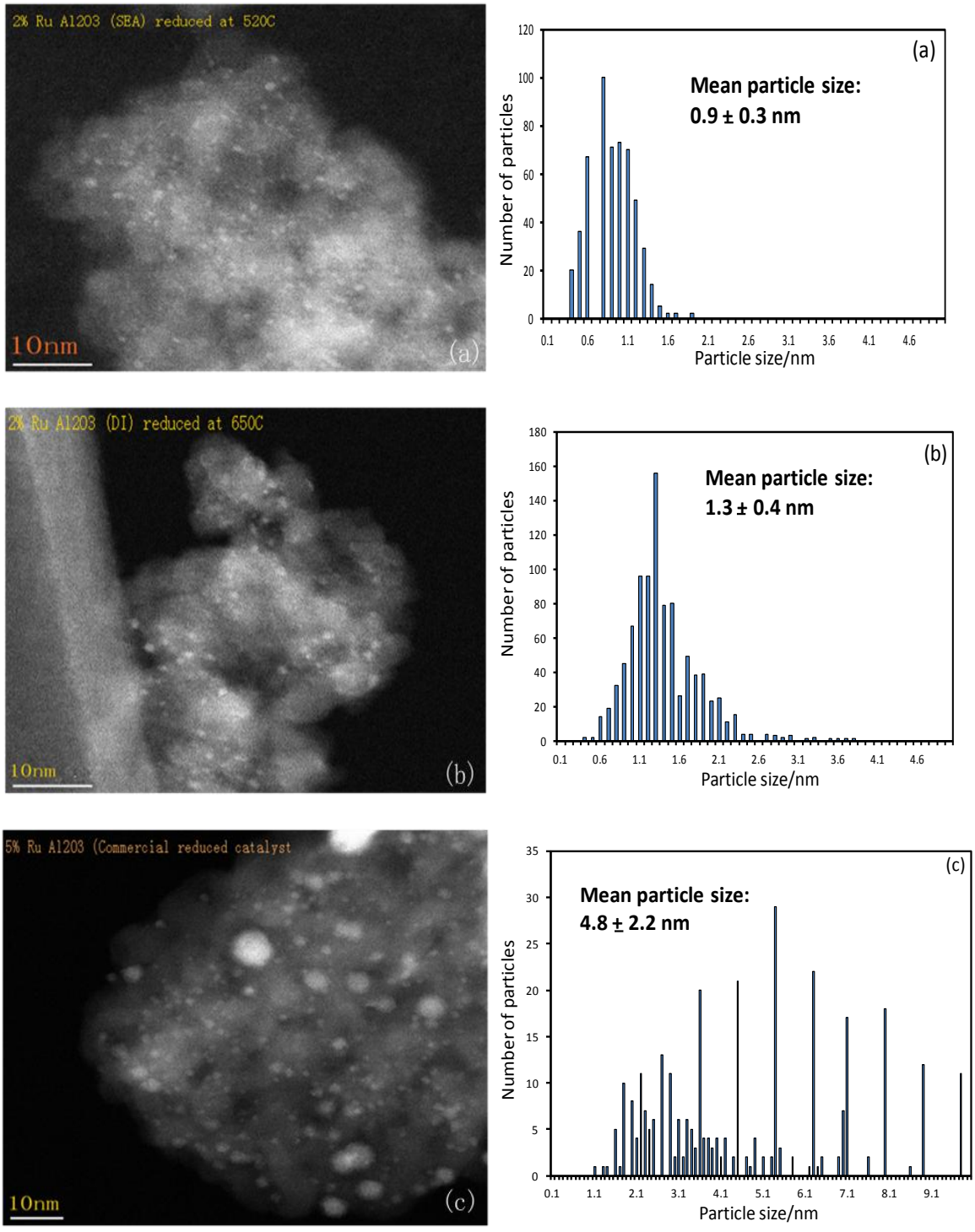

Figure 3.8 Representative STEM images and particle size distributions for Ru catalysts supported on Al_2O_3 after reduction treatment. (a) 2.0% Ru γ-$Al_2O_{3\ SEA}$, (b) 2.0% Ru γ-$Al_2O_{3\ DI}$, (c) 5.5% Ru $Al_2O_{3\ commercial}$.

temperature, likely forming RuO_2. Shown in Fig.3.9 b is the XPS spectrum for the Ru 3p region of 1.5% Ru Cox $_{SEA}$ reduced *in-situ* at 250 ℃.A doublet peak is noticeable in the spectrum with peak binding energy of Ru $3p_{3/2}$ at 462.7ev and Ru $3p_{1/2}$ at 484.5ev, indicating that metallic Ru is formed and that the 1.5% Ru Cox $_{SEA}$ can be completely reduced at 250 ℃.[68]

3.2.6 H_2-O_2 titration chemisorption

Due to the strong interaction between ruthenium and oxygen, metallic Ru can adsorb O_2 on its surface at room temperature, giving oxygen pre-covered Ru particles. This oxide layer can then be titrated with H_2 at 250 ℃ and, through stoichiometric relations, the available active surface of the particles can be calculated, where dispersion of the Ru catalyst can then be determined. Once dispersion is obtained, the ruthenium particle size can also be calculated. The stoichiometry of H_2-O_2 titration chemisorption for Ru catalysts can be proposed such that each Ru atom adsorbs two oxygen atoms which, when reacted with H_2, forms Ru-H and H_2O. Thus, the reaction formula is:

$$O\text{-}Ru\text{-}O+2.5H_2 \longrightarrow Ru\text{-}H+2H_2O \qquad (3\text{-}2)$$

from which the ratio of Ru to H_2 is calculated to be 0.4.[69] In the case of Ru catalysts on carbon, the Ru particle size of 1.5% Ru Cox prepared by SEA is about 3.8nm, 1.5% Ru Cox prepared by DI is about 7.7nm and 5% Ru AC commercial catalyst is about 6.2nm, those are much larger than the particle sizes calculated by XRD and STEM. This big discrepancy between H_2 chemisorption versus XRD and STEM, can possibly be due to carbon decoration over the Ru surface sites, resulting in less amount of oxygen adsorbed on the surface of the Ru particle. For this reason, the dispersion of Ru that was obtained decreased as the am ount of titrated H_2 decreased. One the other hand, for Ru catalysts on

Al_2O_3, the Ru particle size of 2.0% Ru γ-Al_2O_3 $_{SEA}$ is 1.7nm, 2.0% Ru γ-Al_2O_3 prepared $_{DI}$ is 2.5nm, 5% Ru Al_2O_3 is 5.5nm, which is in good agreement with particle sizes determined based on analysis by XRD and STEM.

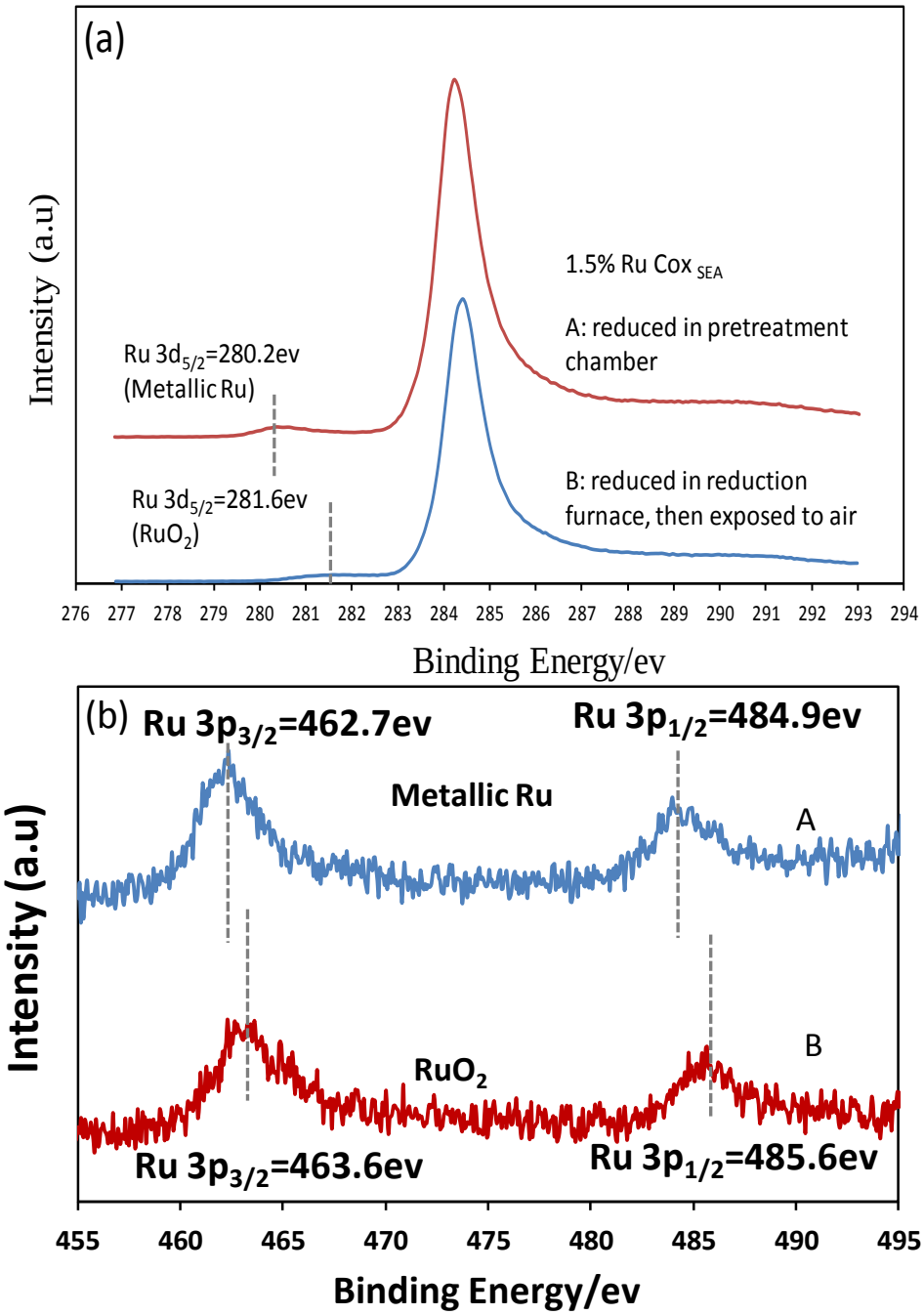

Figure 3.9 (a). XPS spectra for Ru 3d regions of 1.5% Ru Cox $_{SEA}$ (1) after reduction and (2) after reduction and then exposed to air, (b) XPS spectrum for Ru 3p regions of 1.5% Ru Cox $_{SEA}$ after reduction.

3.3 Catalytic activity and Stability of Ruthenium based catalysts

3.3.1 Kinetic Study

3.3.1.1 Determination of the pressure of H_2.

The reactor design is schematized in Fig.4.10. Reaction conditions are P_{total} = 422 psi, T = 220 ℃. The Antoine equation is used to calculate the vapor pressure of solvent (1,4 dioxane) at T = 220 ℃:

$$log_{10} P/bar = A - B/(C + T/K) \quad (3\text{-}3)$$

where A=4.58135, B=1570.093,C=-31.297. Fig. 4.11 shows the vapor pressure of 1,4 dioxane vs temperature. At 220 ℃, the vapor pressure of 1,4 dioxane is 220 psi, thus the pressure of H_2 equals the total pressure less the pressure of 1,4 dioxane = 422 psi – 220 psi = 200 psi.

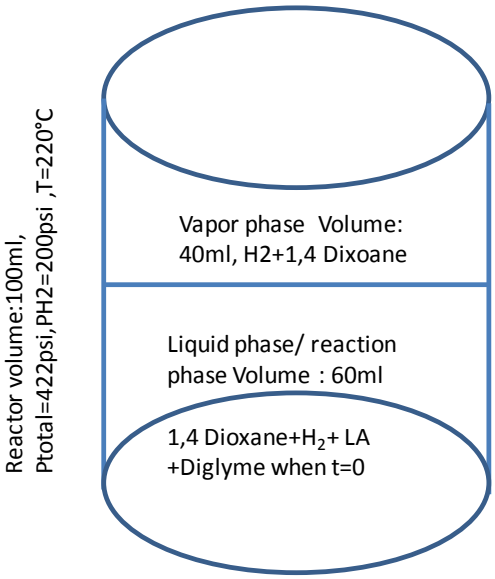

Figure 3.10 Schematic diagram of LA hydrogenation reaction in the batch reactor.

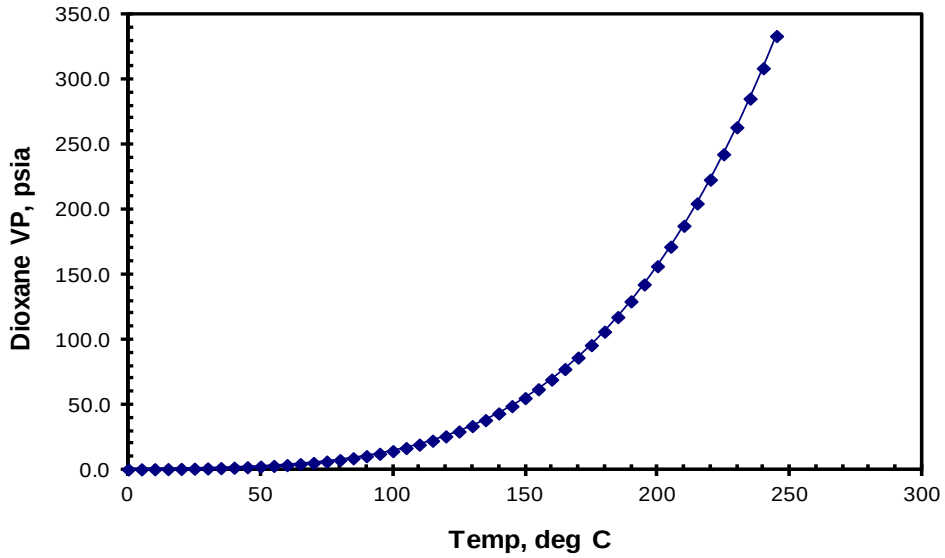

Figure 3.11 Vapor pressure vs. temperature for 1,4 dioxane.

3.3.1.2 Determination of the reaction order of substrate (LA)

The hydrogenation reaction rate can be expressed in a typical power law form as follows:

$$r = -\frac{dc}{dt} = kc^{\alpha}P_{H2}^{\beta} \tag{3-4}$$

Diglyme was used as an internal standard to eliminate injection error. Initial masses of diglyme and LA were 0.2g and 3.0g. Kinetic data of the 5.0% Ru $AC_{commercial}$ catalyst is used as example and is plotted in Fig.3.12a.

The gas chromatography data (Table 4.1) were processed as follows

$$nmoles\ of\ diglyme = \frac{peak\ area * response\ factor\ of\ diglyme}{initial\ weight\ of\ diglyme\ in\ the\ solution * 10}, \tag{3-5}$$

where 10 is a normalization factor used to give normalized values of GVL or LA in a convenient scale (not too large or too small).

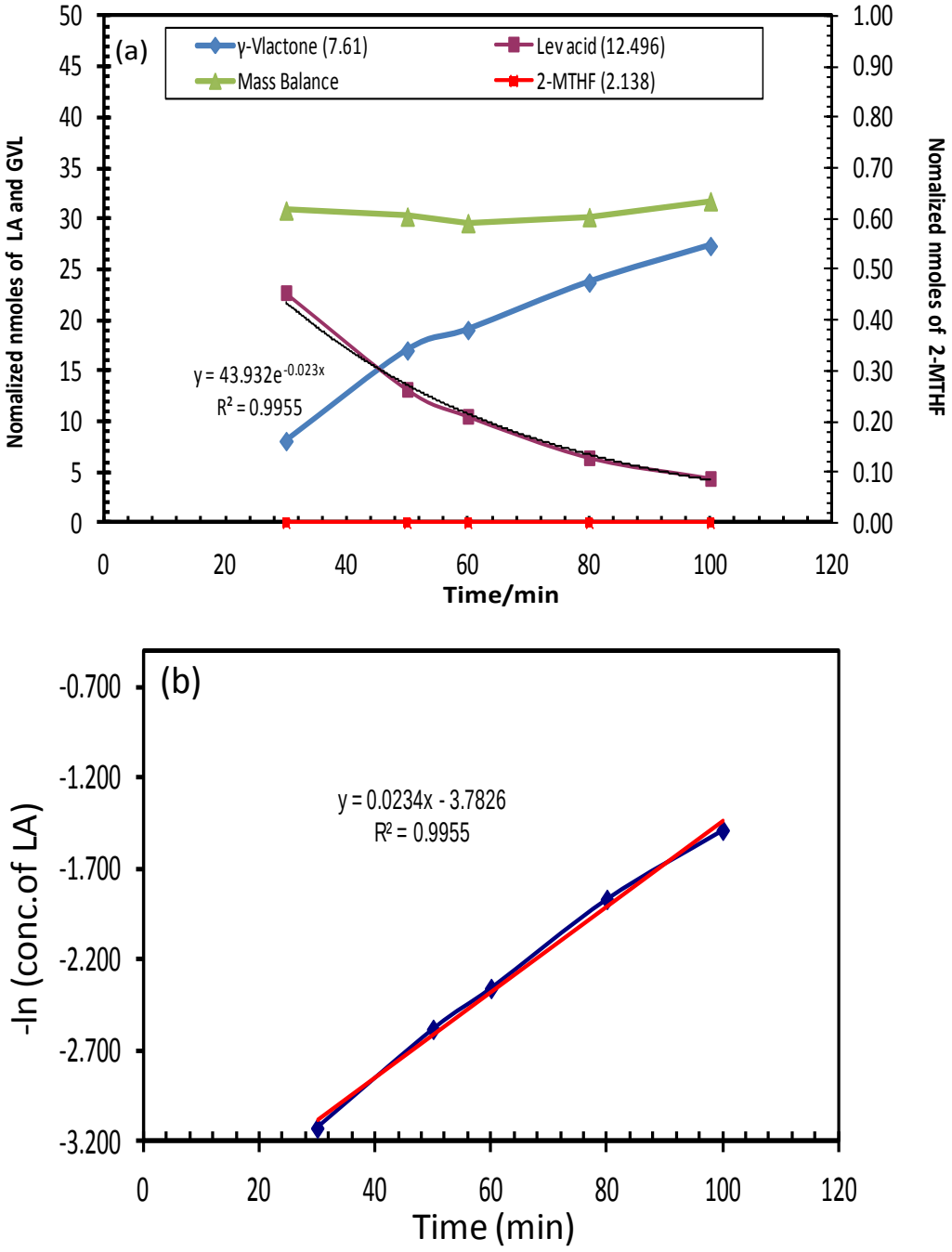

Figure 3.12 (a) Reaction time vs. normalized nmoles of reactant (LA), product (GVL), byproduct (2-MTHF) (b) Reaction time vs. $-\ln C_{LA}$ for hydrogenation of LA to GVL in 360min period run.

$$nomalized\ nmoles\ of\ GVL = \frac{peak\ area * response\ factor\ of\ GVL}{nmoles\ of\ Diglyme}, \quad (3\text{-}6)$$

$$nomalized\ nmoles\ of\ LA = \frac{peak\ area * response\ factor\ of\ LA}{nmoles\ of\ Diglyme}, \quad (3\text{-}7)$$

For instance, at time = 15 mins,

$$nmoles\ of\ diglyme = \frac{99055 * 0.0007136}{0.2011 * 10} = 35.12 \quad (3\text{-}8)$$

$$nomalized\ nmoles\ of\ GVL = \frac{30362 * 0.0007279}{35.12} = 0.63 \quad (3\text{-}9)$$

$$nomalized\ nmoles\ of\ LA = \frac{1830205 * 0.0007813}{35.12} = 40.68 \quad (3\text{-}10)$$

Fig.3.12b presents –ln C e vs. reaction time. The observed linear relation demonstrates that the reaction is 1st order in LA.

Table 3.1 Kinetics data of 5% Ru AC commercial catalyst obtained and analyzed by GC

Number	Time (min)	2-MTHF (2.138)		α-Angelicalactone (5.157)		Diglyme (6.904)		γ-Vlactone (7.61)		Lev acid (12.496)	
		0.0007085		0.0008503		0.0007136		0.0007279		0.0007813	
		Area	nomalized nmoles	Area	nomalized nmoles	Area	nmoles	Area	nomalized nmoles	Area	nomalized nmoles
1	5	3109	0.07		0	89626	31.80	68298	1.56	1683283	41.35
2	15	2866	0.06		0	99055	35.15	30362	0.63	1830205	40.68
3	30	2770	0.06		0	98845	35.07	45971	0.95	1787935	39.83
4	60	2636	0.06		0	90487	32.11	76864	1.74	1601719	38.97
5	90	2594	0.06		0	90731	32.20	106604	2.41	1593693	38.67
6	120	2651	0.05		0	100099	35.52	150247	3.08	1704930	37.50
7	180	2703	0.07		0	75607	26.83	170929	4.64	1186357	34.55
8	240	2911	0.08		0	76290	27.07	225671	6.07	1134765	32.75
9	300	2968	0.06		0	101825	36.13	410000	8.26	1411479	30.52
10	360	2826	0.07		0	86644	30.75	402107	9.52	1095247	27.83

3.3.1.3 Determination of reaction order of pressure of H_2

Due to the low solubility of hydrogen in liquid phase, the reaction usually is performed at high pressure and high hydrogen to reactant mole ratio. It is assumed that the impeller speed is sufficient that any reacted hydrogen is quickly replenished from the gas phase so that the diffusion of H_2 from the gas phase into the liquid is not rate determining. In this way, the amount of H_2 will be large excess compared with LA is there is sufficient hydrogen in the gas phase. The moles of H_2 in the gas phase of the reactor can be calculated by the ideal gas law, where P = 200 psi, V = 40ml, T = 220 ℃ =493 K, and R = 0.08314 (L*bar)/ (K*mol)

$$N = \frac{PV}{RT} = \frac{\left(\frac{200}{145}\right)bar*40*0.001L}{\frac{0.08314(L*bar)}{K*mol}*493K} = 6.6mol \quad (3\text{-}11)$$

$$mol\ of\ LA\ at\ t = 0 = \frac{3g}{116.11} = 0.026mol \quad (3\text{-}12)$$

According to the reaction formula:

$$C_5H_8O_3 + H_2 \rightarrow C_5H_8O_2 + H_2O \quad (3\text{-}13)$$

Therefore, the molar ration hydrogen to LA is ($[H_2]/[LA]=6.6/0.026=254$), which means the reaction rate is independent on the pressure of H_2 ($\beta=0$).

In conclusion, the reaction rate of LA hydrogenation to GVL simplifies as follows:

$$r = -\frac{dc}{dt} = kc^{\alpha}P_{H2}^{\beta} = K_{app}c \quad (3\text{-}14)$$

3.3.1.4 Determination of Activation Energy

To determine the activation energy in our reaction system, 0.25g 5% Ru AC commercial catalyst was used to test activation energy at different temperature at constant hydrogen pressure (200psi) by equation $k = k_0 exp[-Ea/RT]$ (3-15)

where k is rate constant, R=8.314J/mol/K, T is reaction temperature, Ea is apparent activation energy and k_0 is apparent pre-exponential factor. Taking the natural logarithm of equation 3-15, which yields equation

$$lnk = -\frac{Ea}{RT} + lnk_0 \tag{3-16}$$

1/T vs.lnk was plotted in Fig 3.13, where a linear relationship appears and its slope is equal to $-\frac{Ea}{R}$, thus Ea=8.314*4.2906=35.6KJ/mol.

Table 3.2 Reaction rate constant (k) at different temperatures for activation energy determination.

T/℃	T/K	k	T^{-1} (10^{-3}*K^{-1})	lnk
100	373.15	0.00470	2.70	-5.36
130	403.15	0.0162	2.48	-4.12
140	413.15	0.0209	2.42	-3.89
150	423.15	0.0237	2.36	-3.74
160	433.15	0.0250	2.31	-3.69
220	493.15	0.0873	2.03	-2.44

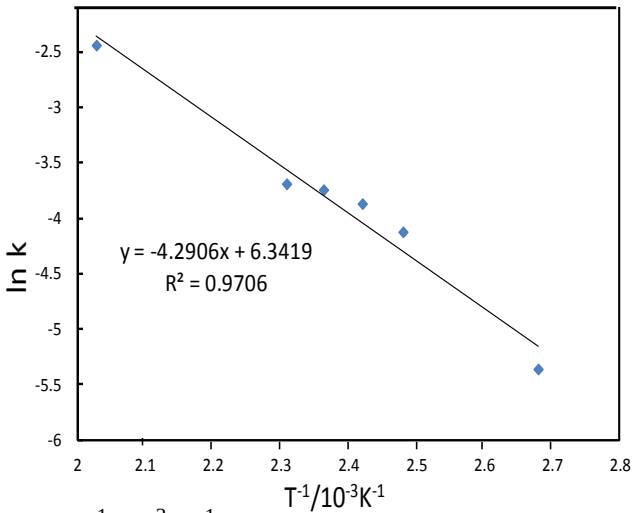

Figure 3.13 Plots of lnk vs.$T^{-1}/10^{-3}$ K^{-1} for activation energy determination.

3.3.2 Catalytic Activity

Hydrogenation of LA to GVL was evaluated over all Ru catalysts to determine the effects of particle size, support type (carbon or alumina) and potassium dopant. In Table 3.3, catalytic activity is reported in terms of reaction rates and turnover frequencies (TOF). Rates were calculated at the time needed for 10% LA conversion and reported as moles of LA converted per gram of Ru per time or moles of LA converted per gram of catalyst per time. For comparison with reaction rates taken from literature review in Table 1.1, moles of GVL produced per gram of Ru per time were also calculated. The TOF is equal to number of moles of converted LA per moles of Ru surface sites per time where the number of active sites is equal to total moles of Ru in each catalyst times its dispersion. Dispersion can be calculated by STEM or chemisorption; both were used.

3.3.2.1 Comparison of activity with reported literature rates

A comparison of measured rates with those reported in the literature is made in Figure 3.14 (a) at the reported conditions. In terms of moles GVL produced per gram of Ru per time, the 4.4% Ru Cox $_{\text{3 time sequential SEA}}$, 1.5% Ru Cox $_{\text{SEA doping K+}}$ and 1.5% Ru Cox $_{\text{SEA}}$ show higher activity than reported literature rates. However, this could be due to the differences in process conditions, namely, the reaction temperature (130 ℃ versus 220 ℃ here), LA concentration (0.43 and 0.36 mol/l versus 0.52 mol/l here), and H_2 pressure (174 and 173psi versus 200 psi here) in references 37 and 34b, respectively. Equation 3-17 and 3-18 can be used to estimate the value of the reaction rate constant at the individual process conditions; these are given in Table 3.4 below.

$$r_A = kC_{LA}C_{H2} \quad (3\text{-}17) \qquad ln\frac{k_2}{k_1} = -\frac{E_a}{R}\left[\frac{1}{T_2} - \frac{1}{T_1}\right] \quad (3\text{-}18)$$

where Ea=35.6kJ/mol calculated from reference 34. T_1=130 ℃, T_2=220 ℃.

Table 3.3 Summary of Ru catalyst activity.

Catalyst	Mass (g)	Particle size (nm)			Rate*10^3 (mol LA)/ (g Ru*s)	Rate*10^5 (mol LA)/ (g catal*s)	TOF/s^{-1} STEM	TOF/s^{-1} chem.
		XRD	STEM	H_2-O_2 titration				
Carbon								
1.5% Ru Cox SEA	0.036	<1.5	1.3	3.8	1.7	2.5	0.22	0.63
4.4% Ru Cox 3 times sequential SEA	0.013	<1.5	1.5	4.5	3.1	14	0.47	1.4
1.5% Ru Cox DI	0.036	3.2	2.1	7.7	0.43	0.65	0.090	0.34
5% Ru AC commercial	0.013	3.3	2.5	6.2	0.54	2.7	0.14	0.36
Alumina								
2% Ru γ-Al_2O_3 SEA	0.036	<1.5	0.9	1.7	0.49	0.96	0.050	0.080
2% Ru γ-Al_2O_3 DI	0.036	<1.5	1.3	2.5	0.88	1.8	0.19	0.23
5% Ru γ-Al_2O_3 commercial	0.013	5.6	4.8	5.5	0.44	2.2	0.21	0.24
K+ dopant								
1.5% Ru Cox SEA doped K+	0.036	<1.5	1.3	4.6	4.4	6.7	0.56	1.98
2% Ru γ-Al_2O_3 SEA doped K+	0.036	<1.5	0.9	1.6	3.1	6.1	0.31	0.52

Blank runs with Cox and γ-Al_2O_3 exhibited negligible activity.

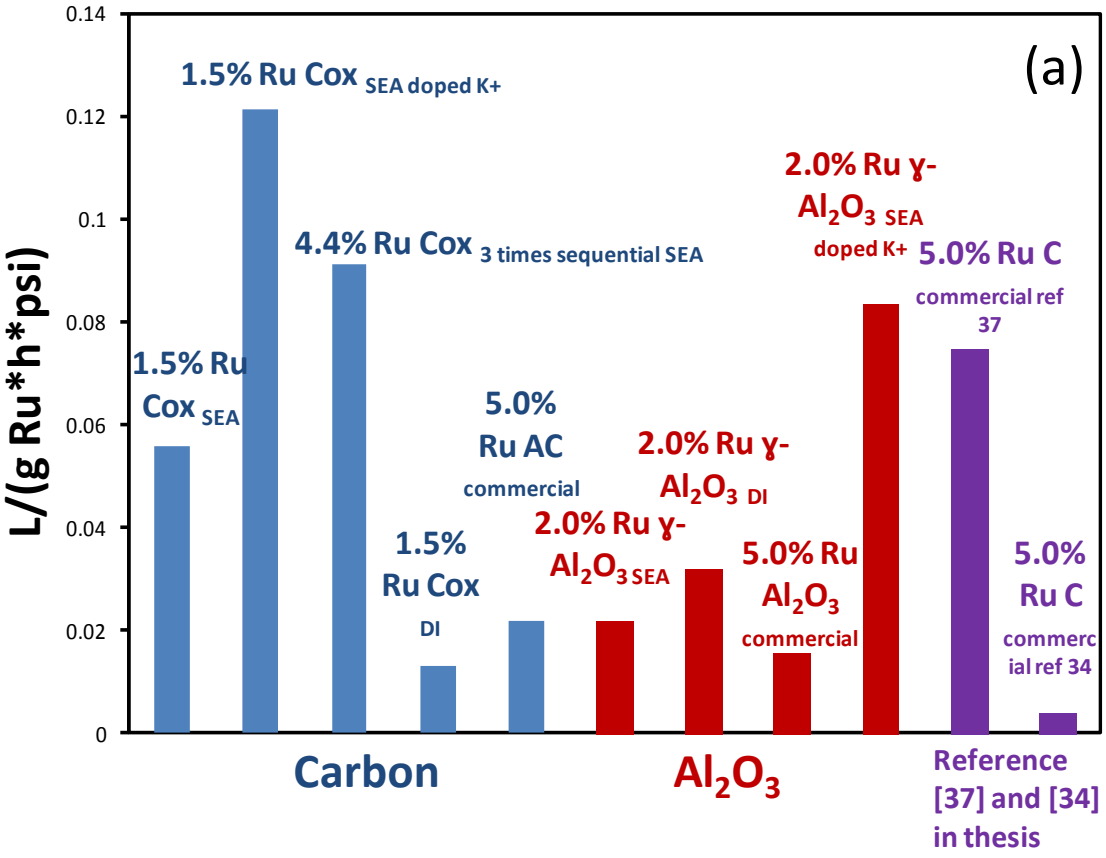

Figure 3.14 (a) GVL production rates of carbon and alumina supported catalysts compared to literature values.

Table 3.4. LA to GVL rate constants of present and literature data.

Catalyst	Ini. Conc. LA (mol/L)	P (psi)	Rate (mol LA/(g Ru*h))	Rate constant at 130 ℃ L/(g Ru*h*psi)	Rate constant at 220 ℃ L/(g Ru*h*psi)
5.0% Ru C commercial ref [37]	0.43	174	1.31	0.0176	0.0747
5.0% Ru C commercial ref [34b]	0.36	173	0.0559	0.000891	0.00378
1.5% Ru Cox SEA	0.52	200	5.79	NA	0.0557
4.4% Ru Cox 3 times sequential SEA	0.52	200	9.47	NA	0.0911
1.5% Ru Cox DI	0.52	200	1.34	NA	0.0129
5.0% Ru AC commercial	0.52	200	2.28	NA	0.0219
2.0% Ru ɣ-$Al_2O_{3\ SEA}$	0.52	200	2.27	NA	0.0218
2.0% Ru ɣ-$Al_2O_{3\ DI}$	0.52	200	3.32	NA	0.0319
5.0% Ru Al_2O_3commercial	0.52	200	1.60	NA	0.0154
1.5% Ru Cox SEA doped K+	0.52	200	12.6	NA	0.121
2.0% Ru ɣ-$Al_2O_{3\ SEA}$ Doped K +	0.52	200	6.88	NA	0.0836

In table 3.4, among all catalysts, the highest rate constant was obtained for 1.5% Ru Cox $_{\text{doped k}}$ catalyst. The commercial carbon supported catalysts tested here and those from the reference [37], display similar reaction rate constant, which provides a convenient benchmark. But rate constant at 220 ℃ converted from the literature [34b] is about 4 times lower than the lowest value reported here. At the same reaction condition, the higher rate constant from literature [37] is still lower than the rate constant obtained from three catalysts prepared by our lab, likely due to the particle size effect and potassium dopant. The support type, particle size, and potassium dopant effects will now be discussed individually.

3.3.2.2 The effect of support: carbon versus alumina

Besides the support effect seen in Figure 3.14 (a), two additional versions of reaction rate results are presented in Figure 3.14 (b) and (c) and reveal the same trend. Figure 3.14 b shows the moles of LA produced per gram of Ru per time, while the moles of LA produced per gram of catalyst per time is plotted in Figure 3.14 c. The common trend of both charts is that 4.4% Ru Cox $_{\text{3 time sequential SEA}}$, 1.5% Ru Cox $_{\text{SEA doping K+}}$, 1.5% Ru Cox $_{\text{SEA}}$ and 2.0 % Ru γ-Al_2O_3 $_{\text{SEA doping K+}}$ show higher activity than the other catalysts. In view of the particle sizes given in Table 3.3, the higher activity per mass of Ru or mass of catalyst for these samples is the result of smaller particle size.

Per mass of Ru, the activity of 1.5% Ru Cox $_{\text{SEA doping K+}}$ is higher than 4.4% Ru Cox $_{\text{3 time sequential SEA}}$ (Fig 3.14b). As both samples had similar particle size (1.3 and 1.5 nm, respectively from Table 3.3), this affect can be attributed to the presence of potassium as discussed below. On the other hand, the activity per mass of catalyst (Fig3.14c), the 4.4% Ru is more active higher due to its higher Ru loading. A general

trend again observed in both plots is the higher activity of carbon supported Ru as compared to Al_2O_3 supported Ru. This supports the findings of Al-Shaal et al [37] and Galletti et al [38], who also found carbon to impart higher activity than alumina.

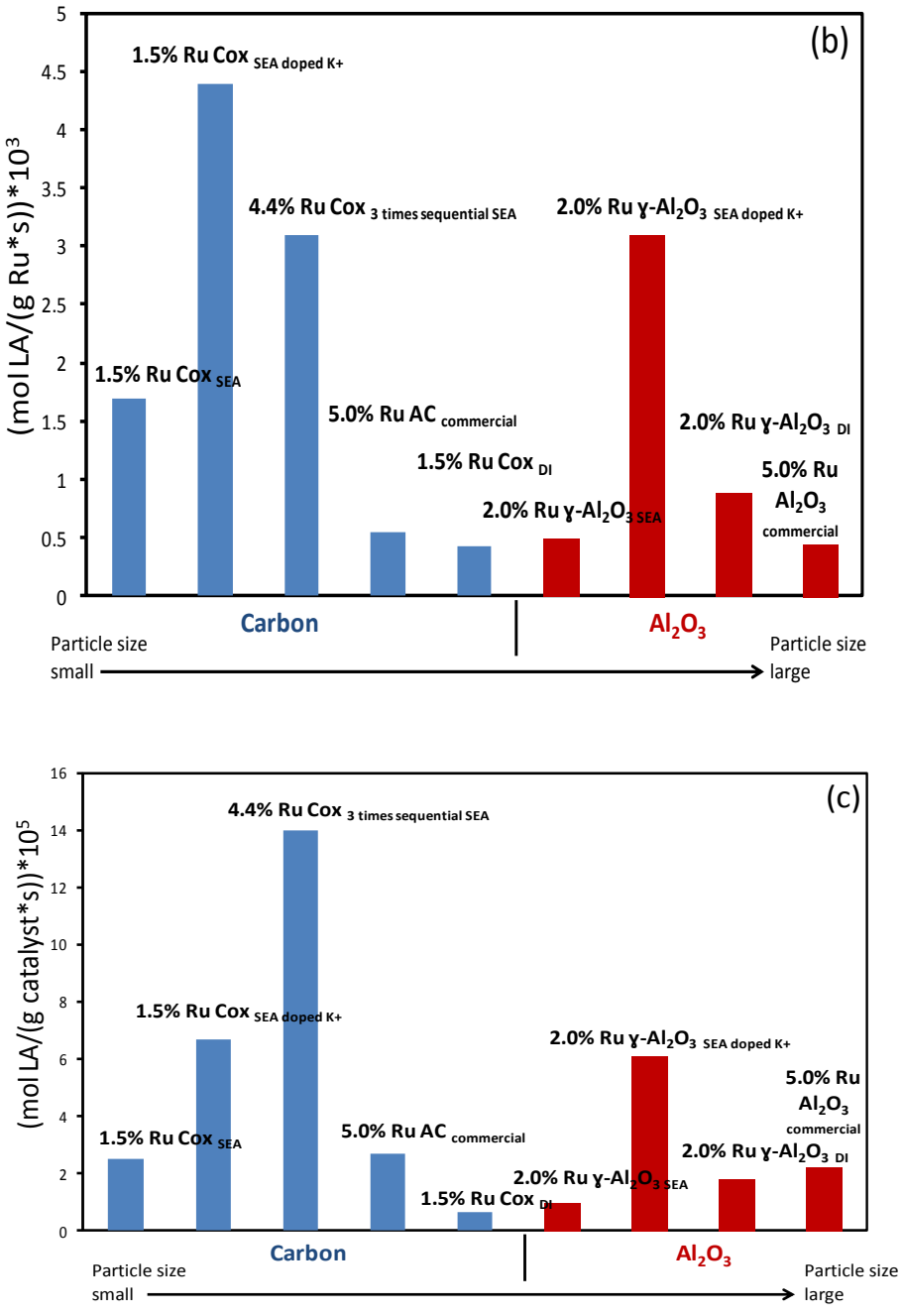

Figure 3.14. (b) rate in terms of mol LA/(gRu*s)*10^3 vs. particle size (c) rate in terms of mol LA/(gRu*s)* 10^5 vs. particle size.

3.3.2.3 The effect of particle size

The effect of particle size can be explored most efficiently with a calculation of turnover frequency and its variation with particle size. These calculations are shown for the carbon and alumina supports in Figures 3.14 d and e, respectively. Calculations based on chemisorption are shown as blue columns, while those based on STEM-based dispersion estimates are shown in red. The TOF values calculated by chemisorption and STEM are significantly different for the carbon based supports as seen in Figure 3.14 d, while the results from the two methods are more consistent for alumina (Figure 3.14 e).

The discrepancy of particle size estimated from the two different characterizations is noteworthy. Estimates from chemisorption are in the range 3.8 – 7.7 nm, which is 2.5 – 4 times larger than the STEM estimates of particle size. Correspondingly, chemisorption extimates of TOF are 2 – 4 times larger than estimates from STEM. That no Ru peaks are evident for the Ru/carbon catalysts in a very sensitive (down to ~1.5 nm particles) powder x-ray diffractometer is consistent with the small size measured by STEM. The current interpretation of this discrepancy, which is being investigated further, is that thin layers of carbon decorate the Ru surface and block a significant fraction of the metal surface. Like potassium promoters, decorating layers of carbon might also have a promotional effect.

A more traditional presentation of the TOF data is shown in Figure 3.14 in which TOF plotted versus particle size for both types of support using chemisorption (Figure 3.14(f) and STEM Figure 3.14(g). The two versions of the plot are consistent for the alumina catalysts: the potassium promoter appears to enhance the activity of Ru, but otherwise the activity appears relatively unaffected by particle size.

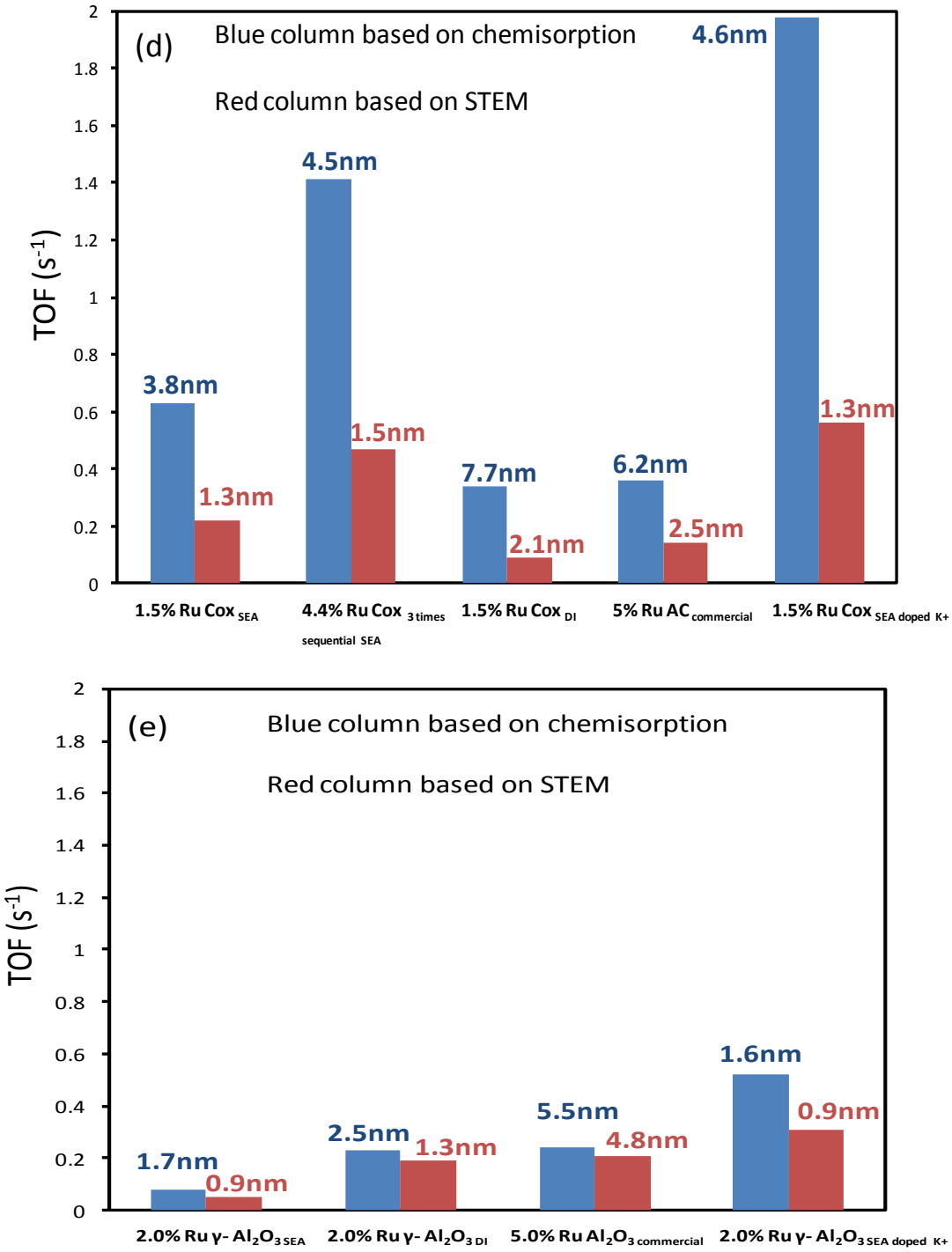

Figure 3.14 (d) TOF vs. carbon support. (e) TOF vs. Al_2O_3 support.

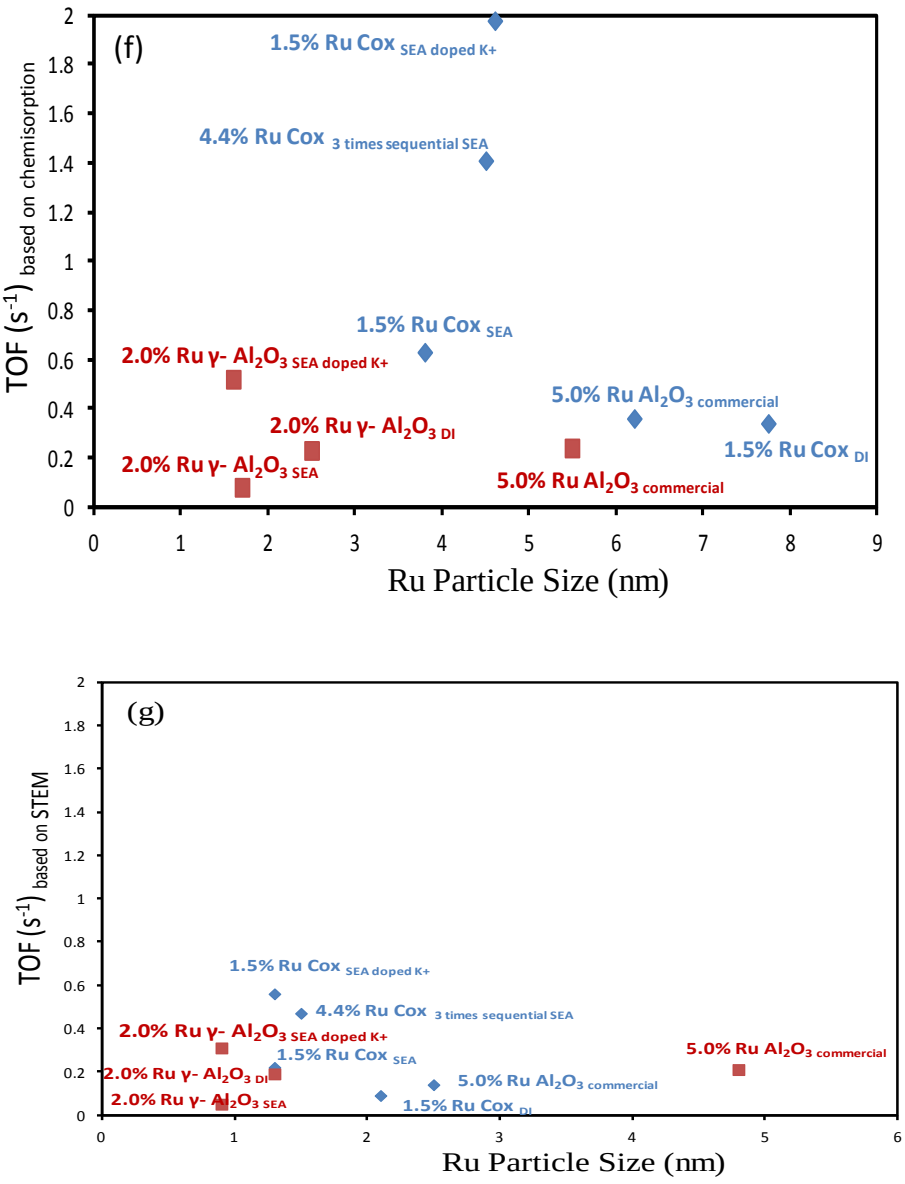

Figure 3.14 TOF versus particle size by f) chemisorption and g) STEM.

The promotion by potassium is also evident in both plots of Figure 3.14 f and g for carbon; the K-doped sample had the highest TOF whether determined by chemisorption or STEM. In the chemisorption-based plot (Figure 3.14 f) there appears to be a sharp volcano of the undoped samples for the 4.4% Ru $Cox_{3\ times\ sequential\ SEA}$ at "4.5" nm. However, since it is know that the size of the particles is much smaller than this, the

enhanced activity can also be attributed to C decoration. A measure of C decoration might be made from the degree of the discrepancy seen in Figure 3.14 d. In that figure, the discrepancy of the 4.4% Ru $Cox_{3\ \text{times sequential SEA}}$ sample (factor of 3) is not appreciably different from the other samples, so nothing can be concluded regarding the decoration effect on activity.

3.3.2.4 The effect of potassium

The effect of potassium was first observed as higher activity of the 2% Ru γ-$Al_2O_{3\ DI}$ compared to the 2.0% Ru γ-Al_2O_3 catalyst, even though the latter catalyst was better dispersed (Table 3.2, 0.9 nm versus 1.3 nm). With the $K_4Ru(CN)_6/\gamma$-Al_2O_3 synthesis, for SEA, only the $[Ru(CN)_6]^{4-}$ complex was adsorbed onto the γ-Al_2O_3.support, as a great excess of liquid is used and is filtered from the solid at the conclusion of the contact time. The vast majority of potassium remains in the filtrate and is separated from the solid. In dry impregnation, however, potassium is doped into the support with the $Ru(CN)_6^{4-}$ complex and stays there as the paste is dried. Proof of this was confirmed by the XPS results shown in Figure 3.15. A doublet peak located at 292.7ev (K $P_{3/2}$) and 295.5ev (K $P_{1/2}$) was observed (δ=2.8ev) for the 2% Ru $Al_2O_{3\ DI}$,[70] but no potassium appeared in 2% Ru $Al_2O_{3\ SEA}$. These results confirm the presence of significant K^+ in the 2% Ru γ-$Al_2O_{3\ DI}$ and the virtual absence of K^+ in the 2% Ru γ-$Al_2O_{3\ SEA}$ catalyst.

It has been reported that potassium can enhance the activity and selectivity for some reactions, such as ammonia synthesis, CO hydrogenation reaction and Fischer-Tropsch synthesis (FTS).[71-73] The mechanism of K promotion for ammonia synthesis over Ru/C is suggested to not only significantly enhance the amount of adsorbed hydrogen, nitrogen and ammonia, but also to weaken the adsorption of strength of those

gases.[74] In the current catalysts, the TPR data of the K-promoted and K-free (DI and SEA preparations, respectively) from Figure 3.16 shows that the K promoter actually retards reduction relative to the K-free preparation, which suggests a weaker interaction of hydrogen with the K-promoted surface.

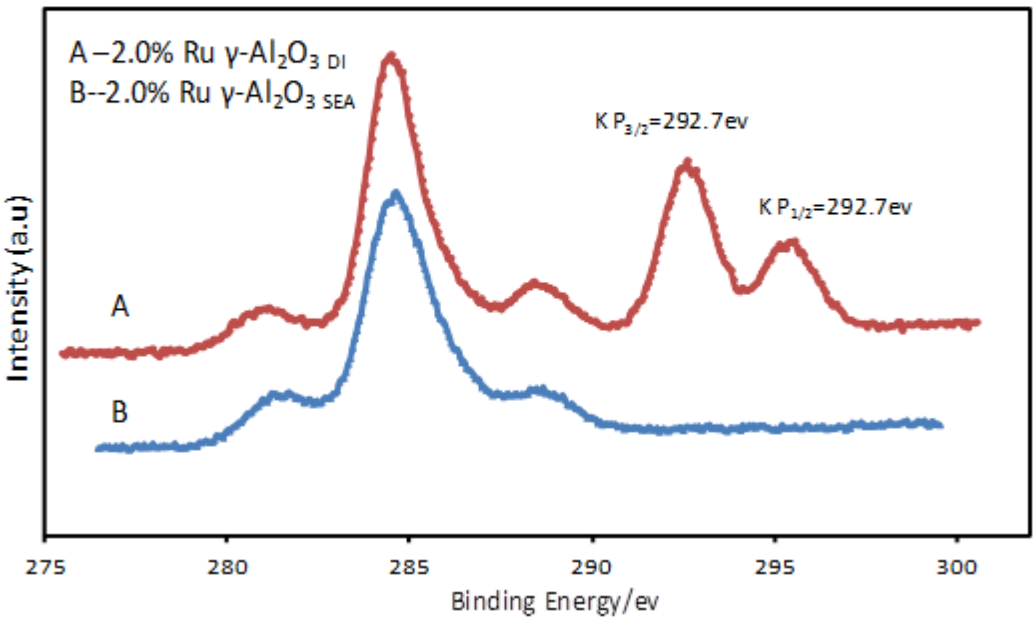

Figure 3.15 XPS spectra of 2% Ru on γ-$Al_2O_{3\ DI}$ and 2% Ru on γ-$Al_2O_{3\ SEA}$ for checking potassium.

On conductive supports such as graphite, the role of K in FTS has been reported as an electron conductor to facilitate the transfer of electrons from the potassium to the ruthenium [73]. The current results exhibit about the same enhancement of rate over both alumina and carbon supports, so it appears that at the current reaction conditions the promotional effect is not related to the conductivity of the support. In fact, the electronic effect on alumina supported Ru is seen in the XPS results of Figure 3.16. The binding

energy of the Ru $3d_{5/2}$ peak shifts from 282.0 eV for the unpromoted catalyst to 281.2eV for the K-promoted sample. This is consistent with the earlier postulation for FTS over Fe [73,75] that the addition of K results in the decrease of activation energy by lowering the local ionization energy in the vicinity of an adsorbed K atom.

To our knowledge, the role of K in hydrogenation of LA has not been published. The enhancement seen in the current results might best be explained by a local decrease in the Ru binding energy to allow increased rates of hydrogen transfer to the adsorbed LA molecule as depicted in Figure 1.6.

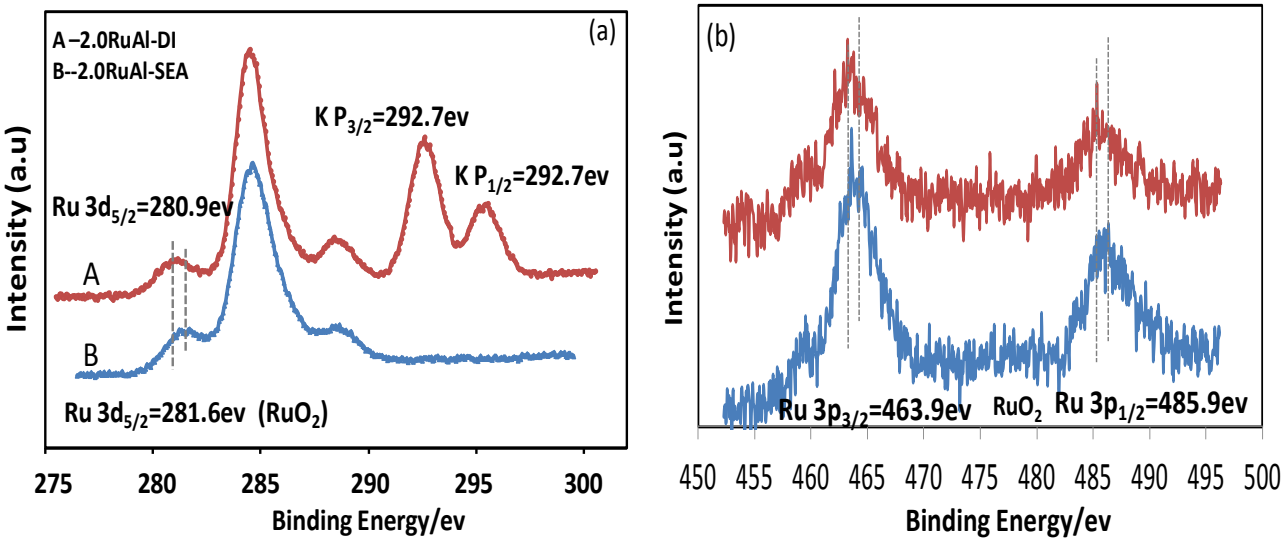

Figure 3.16 K effect on the Ru binding energy.a) XPS of spectra of Ru 3d for 2.0% Ru-ɣ Al_2O_3 DI and 2.0% Ru ɣ-Al_2O_3 SEA (b) XPS of spectra of Ru 3p for 2.0% Ru-ɣ Al_2O_3 DI and 2.0% Ru ɣ-Al_2O_3 SEA.

3.3.3 Stability test of catalysts post reaction

To check whether metal nanoparticle sintering occurs during reaction, XRD was employed for post-reaction characterization. Results for all fresh catalysts show approximately same pattern as the used ones in Fig.3.17, no apparent and sharp Ru metal peaks appear after reaction, which means no significant particle sintering occurs.

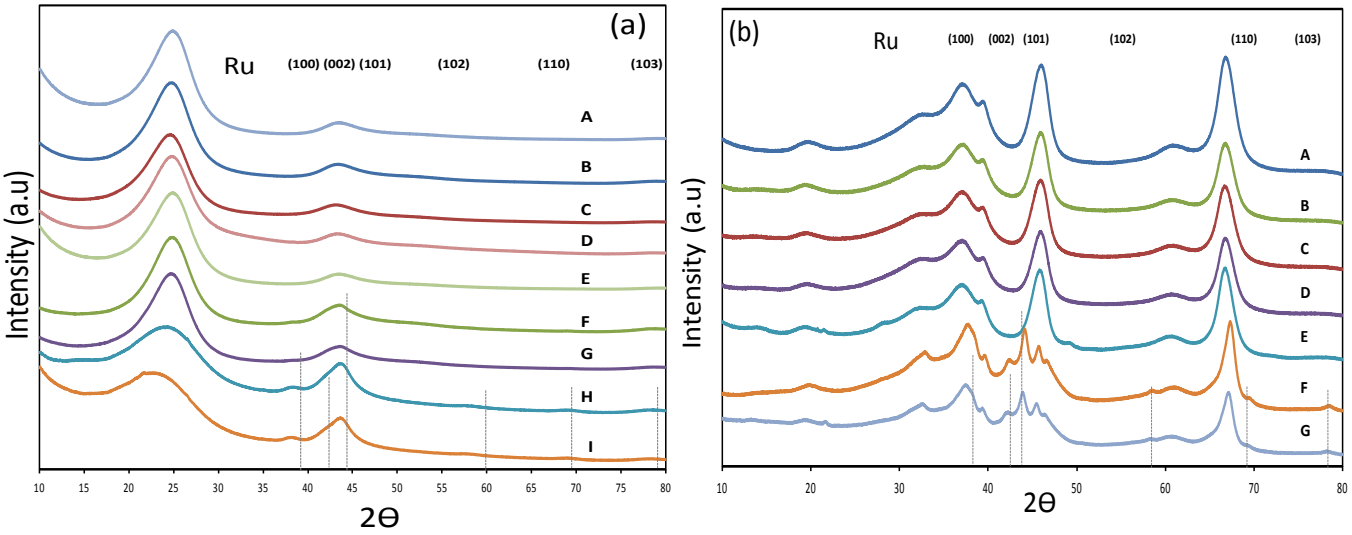

Figure 3.16(a) XRD patterns of Ru catalysts support on Carbon. (A) Cox (B) 1.5% Ru Cox $_{SEA}$ befeore reaction. (C) 1.5% Ru Cox $_{SEA}$ after reaction. (D) 4.4% Ru Cox $_{3\ times\ sequential\ SEA}$ before reaction. (E) 4.4% Ru Cox $_{3\ times\ sequential\ SEA}$ after reaction. (F) 1.5% Ru Cox $_{DI}$ before reaction (G) 1.5% Ru Cox $_{DI}$ after reaction (H) 5.0% Ru AC $_{commercial.}$ before reaction. (I) 5.0% Ru AC $_{commercial.}$ after reaction. (b) (A) γ-Al_2O_3 (B) 2.0% Ru γ-Al_2O_3 $_{SEA}$ befeore reaction. (C) 2.0% Ru γ-Al_2O_3 $_{SEA}$ after reaction. (D) γ-Al_2O_3 (B) 2.0% Ru γ-Al_2O_3 $_{DI}$ befeore reaction. (E) 2.0% Ru γ-Al_2O_3 $_{DI}$ after reaction.(F) 5.0% Ru Al_2O_3 $_{commercial.}$ before reaction.(G) 5.0% Ru Al_2O_3 $_{commercial.}$ after reaction.

Chapter 4. Conclusions and Recommendations

Well dispersed Ru particles were achieved by applying the SEA method supported to both oxidized carbon and γ-Al_2O_3 supports. The surface of oxidized carbon in the aqueous solution at a pH above its PZC (4.0), when the PH of the solution is above the PZC (4.0), becomes deprotonated and negatively charged and able to absorb Ru cations such as Ru $(NH_3)_6^{3+}$. On the other hand, the surface of γ-Al_2O_3 in solutions more acidic it's PZC (8.1), becomes protonated and positively charged and able to absorb the Ru anions, such as Ru $(CN)_6^{4-}$. The maximum uptake of Ru $(NH_3)_6^{3+}$ on oxidized carbon occurs at the final pH of 9.9 and of Ru $(CN)_6^{4-}$ on γ-Al_2O_3 occurs at the final pH 2.1. The maximum surface densities over the respective supports correspond to Ru, metal loadings of 1.6 wt% for Ru/C and about 2.2 wt% for Ru/ γ-Al_2O_3. The Ru particles after reductions were 1.3nm for Ru/C and 0.9nm for Ru/Al_2O_3 as observed with STEM.

Comparison of rates and turnover frequencies of both sets of catalysts displayed two clear trends. First, carbon supported catalysts supported on carbon were generally more active than alumina catalysts. Second, the presence of potassium significantly enhances the activity over either support. This effect was initially detected for the Ru/Al_2O_3 catalyst prepared with $K_4Ru(CN)_6$, and was later confirmed with separate addition of potassium to K-free samples. XPS shows a decrease in the electron binding energy of Ru in the presence of K^+, suggesting that

potassium give rise to an electronic effect in Ru which eases the transfer of hydrogen from Ru to the adsorbed reaction intermediate.

Alumina supported catalysts did not appear to exhibit a particle size effect, as the turnover frequencies calculated on the basis of chemisorption were similar to those estimated from STEM particle size; both sets of numbers did not vary significantly with particle size. On the other hand, a significant discrepancy of particle size estimates via STEM and chemisorption was discovered for the carbon supported catalysts. The unexpectedly low chemisorption uptake is postulated to arise from a decorating layer of carbon in the Ru nanoparticle surfaces. As such, nothing could be concluded about the effect of particle size on TOF for the carbon supported catalysts.

Future work will explore the optimization of amount and type (Na^+, K^+, Cs^+) of alkali promotion. In addition, bimetallic RuRe prepared by Co-SEA and Co-DI will be evaluated and compared with monometallic catalysts.

References

[1] D.M. Alonso, J.Q. Bond, J.A. Dumesic, Green Chem., 12 (2010) 1493-1513.

[2] J.C. Serrano-Ruiz, R. Luque, A. Sepulveda-Escribano, Chemical Society Reviews, 40 (2011) 5266-5281.

[3] E. Chemical, Tomorrow's Energy: A Perspective on Energy Trends, Greenhouse Gas Emissions and Future Energy Options, Exxon Mobil, 2006.

[4] D.M. Alonso, S.G. Wettstein, J.A. Dumesic, Green Chem., 15 (2013) 584-595.

[5] E.L. Kunkes, D.A. Simonetti, R.M. West, J.C. Serrano-Ruiz, C.A. Gärtner, J.A. Dumesic, Science, 322 (2008) 417-421.

[6] D.A. Bulushev, J.R.H. Ross, Catalysis Today, 171 (2011) 1-13.

[7] J.C. Serrano-Ruiz, J.A. Dumesic, Energy & Environmental Science, 4 (2011) 83-99.

[8] P. Azadi, R. Carrasquillo-Flores, Y.J. Pagan-Torres, E.I. Gurbuz, R. Farnood, J.A. Dumesic, Green Chem., 14 (2012) 1573-1576.

[9] P. Gallezot, ChemSusChem, 1 (2008) 734-737.

[10] S.G. Wettstein, J.Q. Bond, D.M. Alonso, H.N. Pham, A.K. Datye, J.A. Dumesic, Applied Catalysis B: Environmental, 117–118 (2012) 321-329.

[11] L. Deng, Y. Zhao, J.A. Li, Y. Fu, B. Liao, Q.X. Guo, ChemSusChem, 3 (2010) 1172-1175.

[12] J.C. Serrano-Ruiz, D.J. Braden, R.M. West, J.A. Dumesic, Applied Catalysis B-Environmental, 100 (2010) 184-189.

[13] P. Kluson, L. Cerveny, Applied Catalysis a-General, 128 (1995) 13-31.

[14] W.R.H. Wright, R. Palkovits, ChemSusChem, 5 (2012) 1657-166

[15] L.E. Manzer, Applied Catalysis A: General, 272 (2004) 249-256.

[16] G.C. Bond, Heterogeneous catalysis: principles and applications, Clarendon Press, 1974.

[17] I.E. Wachs, AIChE Journal, 55 (2009) 284-284.

[18] J.P. Brunelle, Pure and Applied Chemistry, 50 (1978) 1211-1229.

[19] X.R. Zhu, H.R. Cho, M. Pasupong, J.R. Regalbuto, ACS Catalysis, 3 (2013) 625-630.

[20] R. Richards, Surface And Nanomolecular Catalysis, Taylor & Francis Group, 2006.

[21] J.R. Regalbuto, A. Navada, S. Shadid, M.L. Bricker, Q. Chen, Journal of Catalysis, 184 (1999) 335-348.

[22] W.A. Spieker, J.R. Regalbuto, Chemical Engineering Science, 56 (2001) 3491-3504.

[23] X. Hao, W.A. Spieker, J.R. Regalbuto, Journal of Colloid and Interface Science, 267 (2003) 259-264.

[24] L. Jiao, J.R. Regalbuto, Journal of Catalysis, 260 (2008) 329-341.

[25] A. Sepulveda-Escribano, F. Coloma, F. Rodriguez-Reinoso, Applied Catalysis a-General, 173 (1998) 247-257.

[26] J.L. Figueiredo, M.F.R. Pereira, M.M.A. Freitas, J.J.M. Orfao, Carbon, 37 (1999) 1379-1389.

[27] M.A. Fraga, E. Jordao, M.J. Mendes, M.M.A. Freitas, J.L. Faria, J.L. Figueiredo, Journal of Catalysis, 209 (2002) 355-364.

[28] X. Hao, L. Quach, J. Korah, W.A. Spieker, J.R. Regalbuto, Journal of Molecular Catalysis A: Chemical, 219 (2004) 97-107.

[29] S. Lambert, N. Job, L. D'Souza, M.F.R. Pereira, R. Pirard, B. Heinrichs, J.L. Figueiredo, J.P. Pirard, J.R. Regalbuto, Journal of Catalysis, 261 (2009) 23-33.

[30] J. Park, J.R. Regalbuto, Journal of Colloid and Interface Science, 175 (1995) 239-252.

[31] J. Regalbuto, Catalyst Preparation: Science and Engineering, Taylor & Francis, 2006.

[32] M. Schreier, J.R. Regalbuto, Journal of Catalysis, 225 (2004) 190-202.

[33] K.B. Agashe, J.R. Regalbuto, Journal of Colloid and Interface Science, 185 (1997) 174-189.

[34a] Z.P. Yan, L. Lin, S.J. Liu, Energy & Fuels, 23 (2009) 3853-3858. [34b] Y.Gong, L. Lin, Z.P. Yan, BioResources, 6 (2011) 689-699.

[35] P.P. Upare, J.M. Lee, D.W. Hwang, S.B. Halligudi, Y.K. Hwang, J.S. Chang, J. Ind. Eng. Chem., 17 (2011) 287-292.

[36] A.M. Hengne, N.S. Biradar, C.V. Rode, Catal Lett, 142 (2012) 779-787.

[37] M.G. Al-Shaal, W.R.H. Wright, R. Palkovits, Green Chem., 14 (2012) 1260-1263.

[38] A.M.R. Galletti, C. Antonetti, V. De Luise, M. Martinelli, Green Chem., 14 (2012) 688-694.

[39] D.J. Braden, C.A. Henao, J. Heltzel, C.C. Maravelias, J.A. Dumesic, Green Chem., 13 (2011) 1755-1765.

[40] S.G. Wettstein, J.Q. Bond, D.M. Alonso, H.N. Pham, A.K. Datye, J.A. Dumesic, Applied Catalysis B-Environmental, 117 (2012) 321-329.

[41] J. Feng, H. Fu, J. Wang, R. Li, H. Chen, X. Li, Catalysis Communications, 9 (2008) 1458-1464.

[42] C. Liang, Z. Wei, Q. Xin, C. Li, Applied Catalysis A: General, 208 (2001) 193-201.

[43] S. Galvagno, C. Milone, A. Donato, G. Neri, R. Pietropaolo, Catal Lett, 18 (1993) 349-355.

[44] B. Lin, K. Wei, X. Ma, J. Lin, J. Ni, Catalysis Science & Technology, 3 (2013) 1367-1374.

[45] S.-Z. Zheng, X.-Y. Cao, Q. Zhou, S.-H. Wang, G.-S. Hu, J.-Q. Lu, M.-F. Luo, Y.-J. Wang, Journal of Fluorine Chemistry, 145 (2013) 132-135.

[46] L. Oliviero, J Barbier Jr, D. Duprez, A. Guerrero-Ruiz, B. Bachiller-Baeza, I. Rodriguez-Ramos, Applied Catalysis B: Environmental, 25 (2000) 267-275.

[47] C. Crisafulli, S. Scire, R. Zito, C. Bongiorno, Catal Lett, 142 (2012) 882-888.

[48] M. Viniegra, R. Gomez, R.D. Gonzalez, Journal of Catalysis, 111 (1988) 429-432.

[49] K.S. Nagabhushana, E. Dinjus, H. Bönnemann, V. Zaikovskii, C. Hartnig, G. Zehl, I. Dorbandt, S. Fiechter, P. Bogdanoff, J Appl Electrochem, 37 (2007) 1515-1522.

[50] B. Lin, R. Wang, J. Lin, S. Du, X. Yu, K. Wei, Catalysis Communications, 8 (2007) 1838-1842.

[51] A.M. Karim, V. Prasad, G. Mpourmpakis, W.W. Lonergan, A.I. Frenkel, J.G.G. Chen, D.G. Vlachos, J. Am. Chem. Soc., 131 (2009) 12230-12239.

[52] A.C. Basagiannis, X.E. Verykios, Applied Catalysis B: Environmental, 82 (2008) 77-88.

[53] J.M.G. Carballo, J. Yang, A. Holmen, S. García-Rodríguez, S. Rojas, M. Ojeda, J.L.G. Fierro, Journal of Catalysis, 284 (2011) 102-108.

[54] I. Chorkendorff, J.W. Niemantsverdriet, Concepts of Modern Catalysis and Kinetics, Wiley, 2007.

[55] D.H. Everett, R.H. Ottewill, I.U.o. Pure, A. Chemistry, S.o.C. Industry, Surface area determination: proceedings of the International Symposium on Surface Area Determination held at the School of Chemistry, University of Bristol, U.K., 16-18 July, 1969 [organized by] International Union of Pure and Applied Chemistry in conjunction with the Society of Chemical Industry, symposium editors D. H. Everett and R. H. Ottewill, Butterworths, 1970.

[56] S. Lowell, J.E. Shields, Powder surface area and porosity, Chapman and Hall, 1984.

[57] P.W.J.M. Boumans, Inductively Coupled Plasma Emission Spectroscopy: Applications and fundamentals, Wiley, 1987.

[58] M. Che, Characterization of Solid Materials and Heterogeneous Catalysts: From Structure to Surface Reactivity, Wiley-VCH.

[59] A. Jones, B.D. McNicol, Temperature-Programmed Reduction for Solid Materials Characterization, Taylor & Francis, 1986.

[60] .V. ederberg, Thermal conductivity of gases and liquids, Massachusetts, 1965.

[61] R. Guinebreti ère, X-Ray Diffraction by Polycrystalline Materials, Wiley, 2010.

[62] R.M. Lambert, G. Pacchioni, N.A.T.O.S.A. Division, Chemisorption and Reactivity on Supported Clusters and Thin Films:: Towards an Understanding of Microscopic Processes in Catalysis, Springer, 1997.

[63] H.J. H?bschmann, Handbook of GC/MS: Fundamentals and Applications, Wiley, 2009.

[64] R.L. Grob, E.F. Barry, Modern Practice of Gas Chromatography, Wiley, 2004.

[65] X. Ni, B. Zhang, C. Li, M. Pang, D. Su, C.T. Williams, C. Liang, Catalysis Communications, 24 (2012) 65-69.

[66] P.S. Santos, H.S. Santos, S.P. Toledo, Materials Research, 3 (2000) 104-114.

[67] Z.J. Dong, W.Y. Dong, F.Y. Sun, R.S. Zhu, F. Ouyang, Reaction Kinetics Mechanisms and Catalysis, 107 (2012) 231-244.

[68] C.R. Lederhos, P.C. L'Argentiere, F. Coloma-Pascual, N.S. Figoli, Catal Lett, 110 (2006) 23-28.

[69] D.X. Liu, Y.M. Lopez-De Jesus, J.R. Monnier, C.T. Williams, Journal of Catalysis, 269 (2010) 376-387.

[70] A.M. Hibberd, S.L. Bergman, Y.L. Zhong, S.L. Bernasek, The Journal of chemical physics, 137 (2012) 174703-174703.

[71] C.H. Yang, Y.W. Chen, J.G. Goodwin, I. Wender, Abstr. Pap. Am. Chem. Soc., 184 (1982) 22-FUEL.

[72] A. Ozaki, Accounts of Chemical Research, 14 (1981) 16-21.

[73] T.E. Hoost, J.G. Goodwin Jr, Journal of Catalysis, 137 (1992) 22-35.

[74] B.Y. Lin, K.M. Wei, X.F. Ma, J.X. Lin, J. Ni, Catalysis Science & Technology, 3 (2013) 1367-1374.

[75] Z. Paal, G. Ertl, S.B. Lee, Applied Surface Science, 8 (1981) 231-249.